NUMERICAL PREDICTION OF AERODYNAMIC STABILITY DERIVATIVES OF A PROJECTILE

A THESIS SUBMITTED TO
THE GRADUATE SCHOOL OF NATURAL AND APPLIED SCIENCES
OF
MIDDLE EAST TECHNICAL UNIVERSITY

BY

KORAY YAYLA

IN PARTIAL FULFILLMENT OF THE REQUIREMENTS
FOR
THE DEGREE OF MASTER OF SCIENCE
IN
AEROSPACE ENGINEERING

SEPTEMBER 2021

Approval of the thesis:

NUMERICAL PREDICTION OF AERODYNAMIC STABILITY DERIVATIVES OF A PROJECTILE

submitted by **KORAY YAYLA** in partial fulfillment of the requirements for the degree of **Master of Science in Aerospace Engineering Department, Middle East Technical University** by,

Prof. Dr. Halil Kalıpçılar
Dean, Graduate School of **Natural and Applied Sciences** ____________

Prof. Dr. İsmail Hakkı Tuncer
Head of Department, **Aerospace Engineering** ____________

Prof. Dr. Yusuf Özyörük
Supervisor, **Aerospace Engineering, METU** ____________

Examining Committee Members:

Prof. Dr. Sinan Eyi
Aerospace Engineering, METU ____________

Prof. Dr. Yusuf Özyörük
Aerospace Engineering, METU ____________

Prof. Dr. Nafiz Alemdaroğlu
School of Civil Aviation, Atilim University ____________

Assoc. Prof. Dr. Mustafa Kaya
Aerospace Engineering, Ankara Yildirim Beyazit University ____________

Assist. Prof. Dr. Mustafa Perçin
Aerospace Engineering, METU ____________

Date: 07.09.2021

I hereby declare that all information in this document has been obtained and presented in accordance with academic rules and ethical conduct. I also declare that, as required by these rules and conduct, I have fully cited and referenced all material and results that are not original to this work.

Name, Surname: Koray Yayla

Signature :

ABSTRACT

NUMERICAL PREDICTION OF AERODYNAMIC STABILITY DERIVATIVES OF A PROJECTILE

Yayla, Koray
M.S., Department of Aerospace Engineering
Supervisor: Prof. Dr. Yusuf Özyörük

September 2021, 81 pages

Prediction of aircraft aerodynamic stability derivatives is crucial for evaluating its flight dynamic characteristics. By using the open source SU2 software, steady and unsteady Reynolds-Averaged Navier-Stokes analyzes are performed in order to determine the aerodynamic stability derivatives of a missile like projectile from literature. The employed prediction methods that are based on forced oscillatory motion and differential method are particularly emphasized for roll damping and pitch damping derivatives. Also, constant roll rate analyzes are performed with the options of rigid mesh motion and rotating reference frame. Differences between them are evaluated by comparing the results obtained from these different approaches with each other and experimental data. The effects of the Spalart Allmaras and Shear Stress Transport turbulence models on steady and unsteady simulations are examined in terms of accuracy and computational cost. The effects of oscillation method parameters such as reduced frequency, time step size, and oscillation amplitude are also investigated. The numerical prediction of the aerodynamic stability derivatives shows good agreement with the experimental data.

Keywords: stability derivatives, damping derivatives, computational fluid dynamics, forced oscillation method, differential method, rigid mesh motion, rotating reference frame

ÖZ

ROKET TİPİ GEOMETRİLERİN AERODİNAMİK KARARLILIK TÜREVLERİNİN SAYISAL TAHMİNİ

Yayla, Koray
Yüksek Lisans, Havacılık ve Uzay Mühendisliği Bölümü
Tez Yöneticisi: Prof. Dr. Yusuf Özyörük

Eylül 2021 , 81 sayfa

Hava aracı aerodinamik stabilite türevlerinin tahmini, uçuş dinamiği özelliklerini değerlendirmek için çok önemlidir. Açık kaynak kodlu SU2 yazılımı kullanılarak, literatürde yer alan bir füze benzeri mermi geometrisinin aerodinamik kararlılık türevlerini bulmak için daimi ve daimi olmayan akışlarda Reynolds-Averaged Navier-Stokes analizleri yapılmıştır. Zorlanmış salınım hareketine ve diferansiyel yönteme dayanan tahmin yöntemleri, özellikle yuvarlanma ve yunuslama sönümleme türevlerinin hesaplanması için vurgulanmıştır. Ayrıca, rijit ağ hareketi ve dönen referans çerçevesi seçenekleri kullanılarak sabit yuvarlanma hızı altında analizler yapılmıştır. Bu farklı yaklaşımlardan elde edilen sonuçlar birbirleriyle ve deneysel verilerle karşılaştırılarak aralarındaki farklar değerlendirilmiştir. Spalart Allmaras ve Shear Stress Transport türbülans modellerinin daimi ve daimi olmayan akış simülasyonları üzerindeki etkileri, doğruluk ve hesaplama maliyeti açısından incelenmiştir. İndirgenmiş frekans, zaman adımı boyutu ve salınım genliği gibi salınım yöntemi parametrelerinin etkileri de araştırılmıştır. Aerodinamik stabilite türevlerinin sayısal tahmini, deneysel verilerle iyi bir uyum göstermektedir.

Anahtar Kelimeler: kararlılık türevleri, sönümleme türevleri, hesaplamalı akışkanlar dinamiği, zorlanmış salınım yöntemi, diferansiyel yöntem, rijit çözüm ağ hareketi, dönen referans çerçevesi

To my family

ACKNOWLEDGMENTS

I would like to express my sincere thanks to my advisor, Prof. Dr. Yusuf Özyörük, for his support, interest and patience. I would like to thank the members of the jury for listening to me in my thesis defense and for their valuable suggestions.

I would like to thank Roketsan Missiles Inc. for the support throughout my graduate education.

I would like to thank my colleagues Dr. Kaan Görür, Oğuz Han Altıntaş, Özlem Demirel, Hasan Başaran, Uğurtan Demirtaş, Gizem Demirel and my manager Dr. Özgür Ateşoğlu for their support.

I am very proud to have friends like Alp Muhiddinoğlu, Berkan Yerlikaya, Mehmet Başaran and Onur Emre for their encouragement, patience, friendship and kindness.

Also, I would like to thank Derya Kaya, who always helped me when I was in a difficult situation during my graduate education.

Lastly, I would like to thank my family who have always supported me.

The numerical calculations reported in this paper were fully performed at TUBITAK ULAKBIM, High Performance and Grid Computing Center (TRUBA resources).

TABLE OF CONTENTS

LIST OF TABLES

TABLES

LIST OF FIGURES

FIGURES

LIST OF NOTATIONS

α	Angle of Attack
β	Sideslip Angle
δ	Deflection Angle
p	Roll Rate
q	Pitch Rate
r	Yaw Rate
$\dot{\alpha}$	Angle of Attack Rate
$\dot{\beta}$	Sideslip Angle Rate
V	Freestream Velocity
M	Mach Number
Re	Reynolds Number
C_A	Axial Force Coefficient
C_Y	Side Force Coefficient
C_{Y_r}	Side Force Coefficient Derivative with Yaw Rate
C_{Y_β}	Side Force Coefficient Derivative with Sideslip Angle
C_N	Normal Force Coefficient
C_{N_α}	Normal Force Coefficient Derivative with Angle of Attack
$C_{N_{\dot{\alpha}}}$	Translational Normal Force Dynamic Derivative
C_{N_q}	Normal Force Coefficient Derivative with Pitch Rate
C_l	Rolling Moment Coefficient
C_{l_p}	Rolling Moment Coefficient Derivative with Roll Rate
C_m	Pitching Moment Coefficient
C_{m_q}	Pitching Moment Coefficient Derivative with Pitch Rate
C_{m_α}	Pitching Moment Coefficient Derivative with Angle of Attack

$C_{m_{\dot{\alpha}}}$	Translational Pitch Moment Dynamic Derivative
C_n	Yawing Moment Coefficient
C_{n_β}	Yawing Moment Coefficient Derivative with Sideslip Angle
C_{n_r}	Yawing Moment Coefficient Derivative with Yaw Rate
CFD	Computational Fluid Dynamics
3D	3 Dimensional
SA	Spalart-Allmaras
SST	Shear-Stress-Transport
FF	Free Flight
WT	Wind Tunnel
MF	Multiple Fit
SF	Single Fit
SU2	Stanford University Unstructured

CHAPTER 1

INTRODUCTION

1.1 Motivation and Problem Definition

Aerodynamic forces and moments are nonlinear functions of all independent flight conditions such as Mach number (M), altitude (h), angle of attack (α), side slip angle (β), body rotational rates (p, q, r), and control surface settings (δ). It can be assumed that the aerodynamic forces on the aircraft respond linearly to small changes from a given steady-state flight condition. This allows these forces to be characterized by a set of aerodynamic derivatives, called stability derivatives, which are generally used in flight mechanics and flight control studies during aircraft design. Therefore, prediction of aerodynamic stability derivatives of air vehicles is critical to evaluate their flight dynamic characteristics. These derivatives can be obtained by using several different approaches: empirical and semi empirical methods, numerical methods, wind tunnel tests, and flight tests. Wind tunnel tests and flight tests determine aerodynamic stability derivatives accurately. However, they are expensive methods. Also, wind tunnel tests can be limited by scaling, interference factors and blockage. Empirical and semi empirical methods are based on simple mathematical models and theories and existing experimental data. Although semi empirical methods are the fastest and cheapest methods, their accuracy is not sufficient to safely evaluate the flight performance of the vehicles of interest, even in the design process. Also, these methods are insufficient for the aerodynamic solution of complex geometries. Alternatively, numerical methods based on computational fluid dynamics are frequently used considering the accuracy and cost. In this thesis, it is aimed at calculating the aerodynamic stability derivatives accurately, especially dynamic stability derivatives, of missile-like geometries using an open source software Stanford University Unstructured (SU2) Code on unstructured meshes. The results of computational fluid dynamics analyzes conducted for a basic finner projectile from literature are compared with the experimental data and the accuracy of stability derivative prediction methods used in the study is investigated.

1.2 Literature Review

Computational fluid dynamics is a widely used method for finding aerodynamic stability coefficients, which are generally used in flight mechanics and flight control studies during aircraft design. In this section, some studies that have been done and open in literature to calculate stability derivatives are discussed. Before starting computational fluid dynamics methods to determine the stability derivatives, experimental data obtained from wind tunnel tests and flight tests are examined.

Uselton and Jenke [9] conducted a series of wind tunnel experiments from subsonic to supersonic regime to obtain stability derivatives of pitch and roll damping coefficients. They studied on two missile configurations, named basic finner and modified basic finner . Also, Dupuis [2] carried out wind tunnel tests and flight tests to obtain aerodynamic coefficients and stability derivatives at subsonic, transonic and supersonic flight regimes by using the basic finner configuration demonstrated in Figure 1.1 .

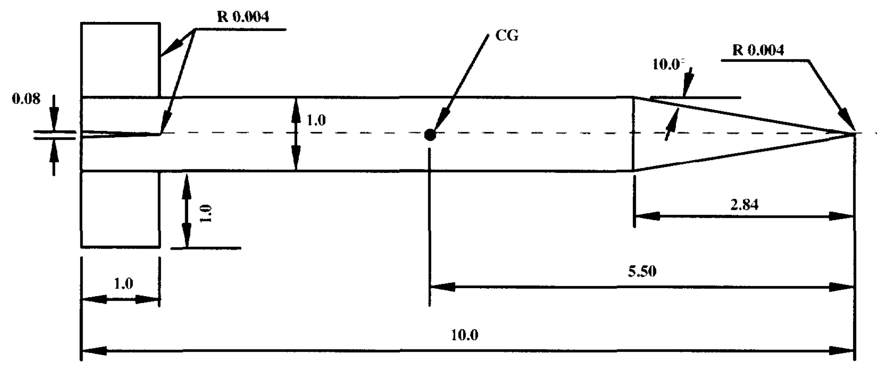

Figure 1.1: Basic finner configuration (all dimensions in caliber) [2].

The Standard Dynamic Model (SDM), shown in Figure 1.2, is also commonly used in the literature. A lot of wind tunnel tests were carried out for different flight conditions to examine the dynamic stability characteristics of a generic aircraft model [10, 11, 12, 13].

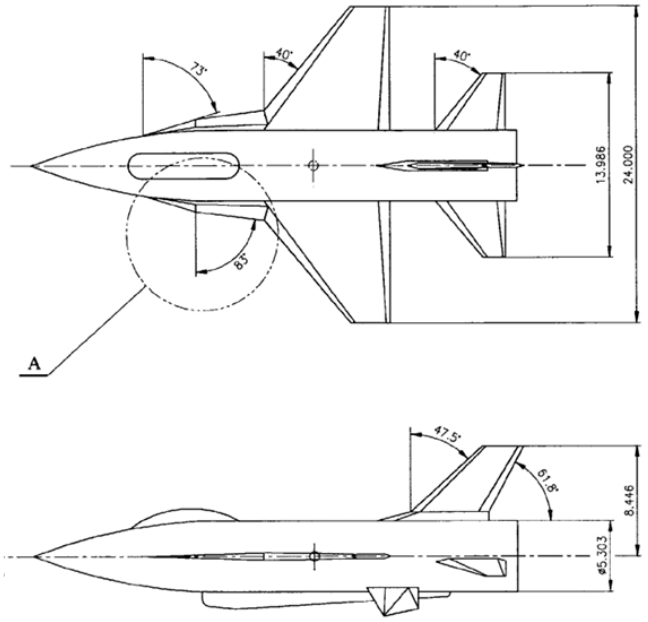

Figure 1.2: SDM model [3].

Vicroy, Loeser and Schütte [4] used a geometry of general unmanned combat aircraft (UCAV) called SACCON:Stability and Control Configuration, indicated in Figure 1.3, to perform static and forced oscillation tests to provide both static and dynamic data in subsonic regime.

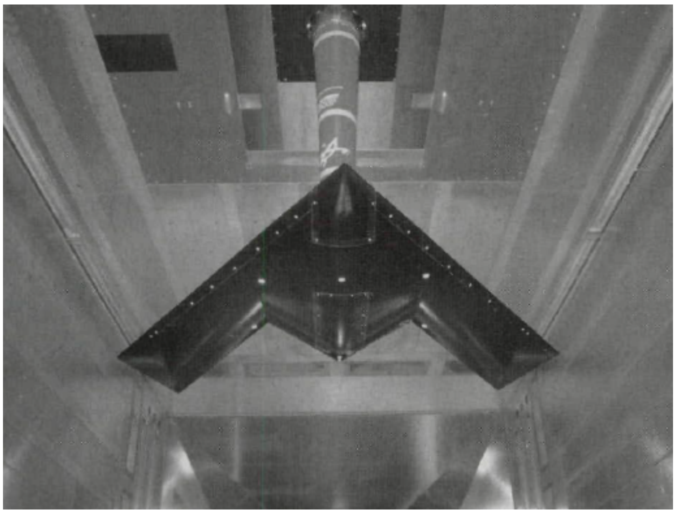

Figure 1.3: Wind tunnel model of SACCON [4].

So far, the models that have available experimental data in the literature have been presented. In this study, the experimental data given for the basic finner model are used as reference. Some other models are also mentioned to raise awareness. Another method used to find stability derivatives, which is the subject of this thesis, is the computational fluid dynamics (CFD). There are many studies that have been done in which static and dynamic derivatives are calculated using CFD.

Oktay and Akay [14] used a three-dimensional unstructured Euler solver for unsteady analysis. They used this solver implemented arbitrary Lagrangian-Eulerian (ALE) formulation with deforming mesh algorithm to predict dynamic derivatives. The roll and pitch damping coefficients were calculated using the history of the aerodynamic force and moment coefficients obtained by the unsteady calculations. They used the basic finner geometry to validate their results at supersonic regime. Their results agreed with the data quite well.

Schmidt and Newman [15] tried to calculate the dynamic stability derivatives of the Standart Dynamic Model (SDM) aircraft model by imposing pitch oscillations. They performed the calculations through a URANS solver with the SST turbulence model. They compared the computed stability derivatives with experimental data. They concluded that the dynamic derivatives calculated at small angles of attack were closer to the experimental data than at high angles of attack due to nonlinear effects caused by vortex shedding.

Bhagwandin and Sahu [7] studied some numerical estimation approaches for pitch damping stability derivatives with CFD. These were called the transient planar pitching method and the steady lunar coning method. The geometries calculated were the basic finner and modified basic finner models. They compared the numerical results with experimental data within subsonic to supersonic regime, and observed that quite accurate results could be obtained.

Ronch [16] carried out a study about the evaluation of dynamic derivatives. The dynamic derivatives were obtained by using unsteady time-domain CFD simulations. In addition, the frequency-domain methods were introduced for the fast computation of dynamic derivatives.

Mi and Zhan [8] proposed a differential method for calculating the aerodynamic damping stability derivatives. They focused on the longitudinal dynamic stability derivatives. They stated that dynamic stability derivatives could be calculated by taking the difference of the solutions obtained from the analyzes performed with different values of flight conditions such as angle of attack, angle of attack rate and pitching angular velocity. They emphasized that this method has higher efficiency and accuracy than traditional oscillating methods. In another study, Baigang, Hao and Ban [17] used small amplitude pitching oscillation and differential method to compute dynamic stability derivatives. Also, they performed small amplitude plunge oscillation to determine the acceleration stability derivative.

Despeyroux et. al. [18] studied static and dynamic performances of a grid fin controlled missile. They carried out the computational fluid dynamic analyzes by using SU2 software. They estimated static stability derivatives, dynamic stability derivatives and aerodynamic coefficients for a general missile with grid fin configuration. They used forced oscillation method in order to predict pitch damping derivatives.

Mi, Zhan and Chen [5] introduced a systematic method based on the step response motion to calculate aerodynamic stability derivatives of an air vehicle by using computational fluid dynamics. The steps of this method are represented in Figure 1.4. After obtaining a steady state solution, the step response motions of angle of attack, angle of attack rate, and pitching angular velocity are employed respectively to predict longitudinal stability derivatives. They used SACCON UCAV model to validate their method. They emphasized that there is a good agreement between aerodynamic coefficients calculated by this method and experimental data. Also, they stated that this method can provide advantages in terms of computational cost and accuracy with respect to traditional methods [5].

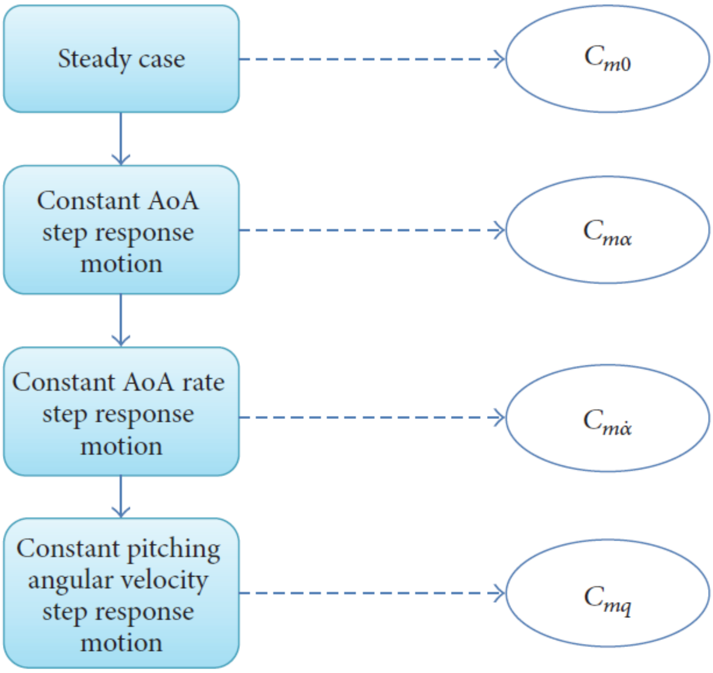

Figure 1.4: Simulation steps of the method based on step response motion [5].

1.3 The Outline of the Thesis

The methodology used to predict aerodynamic stability derivatives by using computational fluid dynamics is explained in the second chapter. In the third section, by choosing the appropriate mesh and solver settings, the computations with the open source SU2 software is validated by comparing with the experimental data of the basic finner model. The calculations of aerodynamic stability derivatives using the methodology described in the second chapter are presented and discussed in the fourth chapter. The findings to calculate stability derivatives by using computational fluid dynamics are summarized in the last part of the thesis.

CHAPTER 2

METHODOLOGY

In this section, the methodology in order to calculate aerodynamic stability derivatives is explained. Firstly, the numerical methodology used in this study is described. The governing equations solved in the CFD phase are given. Turbulence models employed in the analyzes are described. Then, the prediction methods of aerodynamic the stability derivatives are represented. Since there are experimental results of the roll damping and pitch damping coefficients, the determination of these coefficients are especially emphasised to evaluate the accuracy of the numerical prediction methods.

2.1 Numerical Methodology

All computational fluid dynamic analyzes are carried out by using the open source SU2 [19] v7.1.1 "Blackbird" software. The aerodynamic coefficients are calculated solving the compressible, 3D, Reynolds-Averaged Navier-Stokes (RANS) equations. The numerical method employed for the convective terms is chosen as the Jameson Schmidt Turkel (JST) scheme. In order to model turbulence, the model of Spalart Allmaras (SA) and the model of Shear Stress Transport (SST) of Menter are alternatively employed. Second order dual-time-stepping is selected for time integration.

2.2 Reynolds-Averaged Navier-Stokes (RANS) Equations

The Reynolds-Averaged Navier-Stokes equations expressed in arbitrary Lagrangian-Eulerian (ALE) [20] differential form, as used in the SU2 code, is given as [21];

$$\begin{cases} \mathcal{R}(U) = \frac{\partial U}{\partial t} + \nabla \cdot \vec{F}^{c}_{\text{ale}} - \nabla \cdot \vec{F}^{v} - \mathcal{Q} = 0 & \text{in } \Omega, \quad t > 0 \\ \vec{v} = \vec{u}_{\Omega} & \text{on } S \\ \partial_n T = 0 & \text{on } S \\ (W)_{+} = W_{\infty} & \text{on } \Gamma_{\infty} \end{cases} \tag{2.1}$$

where $\vec{F}^{c}_{ale}$ and $\vec{F}^{v}$ are the viscous fluxes and the convective fluxes, respectively. $\mathcal{Q}$ is defined as generic source term. The conservative variables are represented by $U = \{\rho, \rho\vec{v}, \rho E\}^{\top}$.

In equation (2.1), $\Omega \subset \mathbb{R}^3$ defines the domain, Γ_{∞} and S define far-field boundary and adiabatic wall boundary, respectively.

The formulation of convective fluxes, viscous fluxes and source term are given as;

$$\begin{gathered} \vec{F}^{c}_{alc} = \left\{ \begin{array}{c} \rho\left(\vec{v} - \vec{u}_{\Omega}\right) \\ \rho\vec{v} \otimes \left(\vec{v} - \vec{u}_{\Omega}\right) + \bar{I}p \\ \rho E\left(\vec{v} - \vec{u}_{\Omega}\right) + p\vec{v} \end{array} \right\} \\ \vec{F}^{v} = \left\{ \begin{array}{c} \cdot \\ \bar{\bar{\tau}} \\ \bar{\bar{T}} \cdot \vec{v} + \mu^{*}_{\text{tot}}\, c_p \nabla T \end{array} \right\} \\ \mathcal{Q} = \left\{ \begin{array}{c} q_{\rho} \\ \vec{q}_{\rho v} \\ q_{\rho E} \end{array} \right\} \end{gathered} \tag{2.2}$$

where $\vec{v} = \{v_1, v_2, v_3\}^{\top}$ is the flow speed in Cartesian frame and $\vec{u}_{\Omega}$ is the moving domain velocity. ρ, p, T and E denote the density, the static pressure, the temperature and the total energy per unit mass respectively. c_p is defined as the specific heat constant under constant pressure. μ and $\bar{\bar{\tau}}$ are the viscosity and the viscous stress tensor respectively [21].

The viscous stress tensor can be expressed as;

$$\overline{\overline{\tau}} = \mu_{tot}\left(\nabla\vec{v} + \nabla\vec{v}^{\top} - \frac{2}{3}\overline{\overline{I}}(\nabla\cdot\vec{v})\right) \tag{2.3}$$

The viscosity (μ_{tot}) can be split into dynamic (μ_{dyn}) and turbulent (μ_{tur}) components as shown in equation (2.4). While the dynamic viscosity is obtained by using Sutherland's law, the turbulent viscosity is calculated with a turbulence model [21].

$$\mu_{tot} = \mu_{dyn} + \mu_{tur} \tag{2.4}$$

2.3 Turbulence Modeling

Two common turbulence models of the Spalart Allmaras (SA) and the Menter Shear Stress Transport (SST) are explained in this part.

2.3.1 Spalart-Allmaras (SA) Model

The Spalart–Allmaras (SA) turbulence model uses a one-equation that solves the transport equation for turbulent viscosity. The turbulent viscosity is computed by using the following equations [21].

$$\mu_{tur} = \rho\hat{\nu}f_{v1}, \quad f_{v1} = \frac{\chi^3}{\chi^3 + c_{v1}^3}, \quad \chi = \frac{\hat{\nu}}{\nu}, \quad \nu = \frac{\mu_{dyn}}{\rho} \tag{2.5}$$

In the equation (2.5), $\hat{\nu}$ is calculated by using a transport equation. The terms of convective fluxes ($\vec{F}^{c}$), viscous fluxes ($\vec{F}^{v}$), and source (Q) in the transport equation are defined as [21];

$$
\begin{aligned}
\vec{F}^{c} &= \vec{v}\hat{\nu} \\
\vec{F}^{v} &= -\frac{\nu+\hat{\nu}}{\sigma}\nabla\hat{\nu} \\
Q &= c_{b1}\hat{S}\hat{\nu} - c_{w1}f_{w}\left(\frac{\hat{\nu}}{d_{S}}\right)^{2} + \frac{c_{b2}}{\sigma}|\nabla\hat{\nu}|^{2}
\end{aligned}
\tag{2.6}
$$

For detailed information about the variables and functions in transport equation, references [21] and [22] can be referred.

2.3.2 Menter Shear Stress Transport (SST) Model

The Menter Shear Stress Transport (SST) model is a two equation turbulence model which consists of specific dissipation rate (ω) and turbulence kinetic energy (k). In this model, a shear stress limiter is implemented to the eddy-viscosity relationship which is defined as [21];

$$
\mu_{\text{tur}} = \frac{\rho a_{1} k}{\max\left(a_{1}\omega, SF_{2}\right)}, S = \sqrt{2S_{ij}S_{ij}}
\tag{2.7}
$$

where F_2 is called as the second blending function.

The terms of convective, viscous and sources for the equation of turbulence kinetic energy are given in equation (2.8).

$$
\begin{aligned}
\vec{F}^{c} &= \rho k\vec{v} \\
\vec{F}^{v} &= -\left(\mu_{\text{dyn}} + \sigma_{k}\mu_{\text{tur}}\right)\nabla k \\
Q &= P - \beta^{*}\rho\omega k
\end{aligned}
\tag{2.8}
$$

The convective, viscous and source terms for the equation of specific dissipation rate are given in equation (2.9).

$$\begin{aligned}\vec{F}^c &= \rho\omega\vec{v} \\ \vec{F}^v &= -\left(\mu_{\text{dyn}} + \sigma_\omega \mu_{tur}\right)\nabla\omega \\ Q &= \frac{\gamma}{\nu_t}P - \beta^*\rho\omega^2 + 2\left(1 - F_1\right)\frac{\rho\sigma_{\omega 2}}{\omega}\nabla k \nabla\omega\end{aligned} \tag{2.9}$$

where P is the turbulent kinetic energy production and F_1 is the first blending function.

For more detailed information about the variables and functions used in the Menter SST model, [21] and [23] can be referred to.

2.4 Dynamic Mesh Definition

SU2 has the capability of resolving unsteady flows on with meshes that are both rigidly transformed and dynamically deformed [21]. The rigid mesh motion without any relative movement between the grid nodes as shown in Figure 2.1 is a simpler way to move the surfaces and the mesh. Mesh velocities, including dynamic grid motion, are calculated and used in the governing equations in the unsteady simulations with movement of surfaces. The rigid mesh motion, which includes both rotation and translation, for each grid node, can be defined as [24]:

$$\vec{x}_{n+1} = \Re\vec{x}_n + \Delta\vec{x} \tag{2.10}$$

where $\vec{x}_n$ is the current position of the nodes, $\vec{x}_{n+1}$ is the updated position of the nodes at the next time step, $\Delta\vec{x}$ is the vector that states the translation of the nodal coordinates and $\Re$ is the rotation matrix which can be expressed as [24];

$$\Re = \begin{bmatrix} c\theta_y c\theta_z & s\theta_x s\theta_y c\theta_z - c\theta_x s\theta_z & c\theta_x s\theta_y c\theta_z + s\theta_x s\theta_z \\ c\theta_y s\theta_z & s\theta_x s\theta_y s\theta_z + c\theta_x c\theta_z & c\theta_x s\theta_y s\theta_z - s\theta_x c\theta_z \\ -s\theta_y & s\theta_x c\theta_y & c\theta_x c\theta_y \end{bmatrix} \tag{2.11}$$

where θ_x, θ_y and θ_z define the change in angular position of the coordinates of the grid nodes about a specified rotation center.

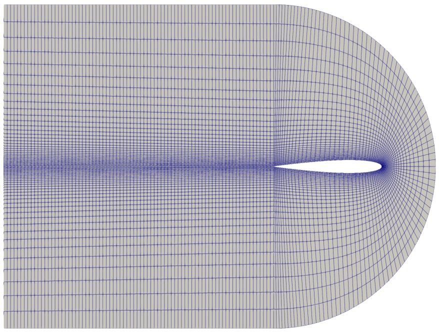

(a) Initial mesh.

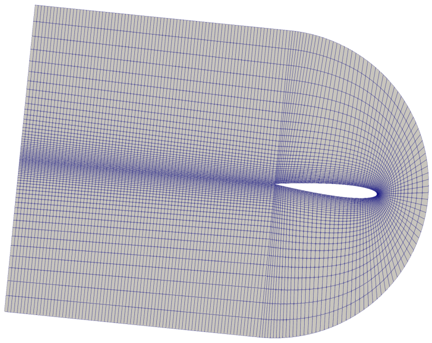

(b) Mesh after rigid motion.

Figure 2.1: Rigid mesh motion.

Figure 2.2 shows dynamically deformed mesh. When using the deforming mesh option, the volume mesh is deformed after moving the surface boundary. Calculating the mesh deformation leads to increase in computational cost. Also, mesh quality may deteriorate as the mesh deforms. Therefore, the rigid mesh motion is preferred in this study.

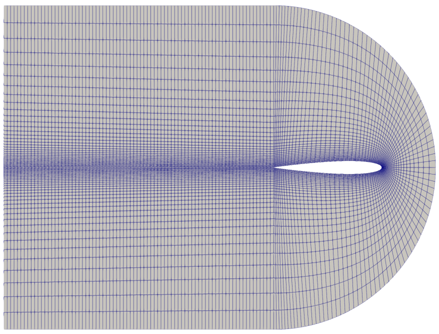

(a) Initial mesh.

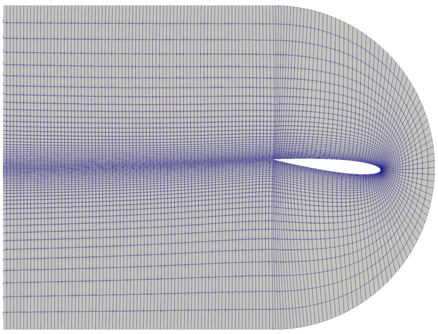

(b) Mesh after deforming surface movement.

Figure 2.2: Deforming mesh motion.

2.5 Rotating Frame Formulation

Transforming the flow equations into a reference frame that rotates with the body can be advantageous for simulations under steady rotation since flow field can be solved in a steady manner without any grid movement [24]. By applying this transformation with a steady angular velocity $\vec{\omega} = (\omega_1, \omega_2, \omega_3) \in \mathbb{R}^3$ around a specified rotation center $\vec{r}_o = (x_o, y_o, z_o) \in \mathbb{R}^3$, the convective fluxes of the compressible equations become;

$$\vec{F}^c = \begin{pmatrix} \rho\left(\vec{v} - \vec{u}_r\right) \\ \rho\vec{v} \otimes \left(\vec{v} - \vec{u}_r\right) + \bar{\bar{I}}P \\ \rho H\left(\vec{v} - \vec{u}_r\right) + P\vec{u}_r \end{pmatrix}, Q = \begin{pmatrix} 0 \\ -\rho(\vec{\omega} \times \vec{v}) \\ 0 \end{pmatrix} \tag{2.12}$$

where ρ, H and P are the fluid density, total enthalpy per unit mass, and static pressure, respectively. $\vec{v} = (v_1, v_2, v_3) \in \mathbb{R}^3$ is defined as the absolute flow velocity and $\vec{u}_r$ is the velocity due to rotation, sometimes called whirl velocity. $\vec{u}_r$ can be formulated as;

$$\vec{u}_r = \vec{\omega} \times \vec{r} \tag{2.13}$$

where $\vec{r}$ is defined as the position vector from the center of rotation to a point in the flow domain, as represented in the following equation.

$$\vec{r} = \left(\left(x - x_o\right), \left(y - y_o\right), \left(z - z_o\right)\right) \tag{2.14}$$

The viscous terms do not change during the transformation from inertial frame to rotating frame.

2.6 Stability Derivative Calculation Methods

In general, aerodynamic force and moment coefficients are nonlinear functions of the flight conditions such as velocity, altitude, angle of attack, sideslip angle, body rotational rates, and the geometry such as control surface settings. However, for simplification, assuming linearity and using Taylor series expansion, aerodynamic coefficients at constant velocity, altitude and geometry can be assumed as a function of all individual parameters as shown in equation (2.15) [1]. Higher order terms in Taylor series expansion of the parameters are assumed to be negligible.

$$\begin{aligned} C_j = C_{j0} + \frac{\partial C_j}{\partial \alpha}\Delta\alpha + \frac{\partial C_j}{\partial \dot{\alpha}}\Delta\dot{\alpha} + \frac{\partial C_j}{\partial \beta}\Delta\beta + \frac{\partial C_j}{\partial \dot{\beta}}\Delta\dot{\beta} \\ + \frac{\partial C_j}{\partial p}\Delta p + \frac{\partial C_j}{\partial q}\Delta q + \frac{\partial C_j}{\partial r}\Delta r \end{aligned} \tag{2.15}$$

where $j = A, N, Y, l, m, n$.

A, N and Y define the coefficients of axial force, normal force and side force while l, m and n represent the coefficients of roll moment, pitch moment and yaw moment respectively.

When rotational motions about the axis of the body frame are small amplitude angular displacements, θ_x, θ_y and θ_z, the angular velocity of the body can be expressed as [1];

$$\Delta p = \dot{\theta}_x, \quad \Delta q = \dot{\theta}_y, \quad \Delta r = \dot{\theta}_z \tag{2.16}$$

The relationship between the angular velocity resolved in the wind frame (ω_x, ω_y, ω_z) and the angular velocity resolved in the body frame ($\dot{\theta}_x$, $\dot{\theta}_y$, $\dot{\theta}_z$) is given as [1];

$$\begin{bmatrix} \omega_x \\ \omega_y \\ \omega_z \end{bmatrix} = \begin{bmatrix} \cos\alpha\cos\beta & \sin\beta & \sin\alpha\cos\beta \\ -\cos\alpha\sin\beta & \cos\beta & -\sin\alpha\sin\beta \\ -\sin\alpha & 0 & \cos\alpha \end{bmatrix} \begin{bmatrix} \dot{\theta}_x \\ \dot{\theta}_y \\ \dot{\theta}_z \end{bmatrix} \tag{2.17}$$

The body frame (x_b, y_b, z_b) and wind frame (x_w, y_w, z_w) are demonstrated in Figure 2.3. The origin of both frames is located at the center of gravity. The body x axis (x_b) points through to the nose. The body z axis (z_b) points down and y_b points through the right tail. The wind x axis (x_w) is in the same direction as the velocity vector $\vec{V}$. The y_w and z_w axis of the wind frame can be defined by the transformation using the angle of attack α and the angle of side slip β.

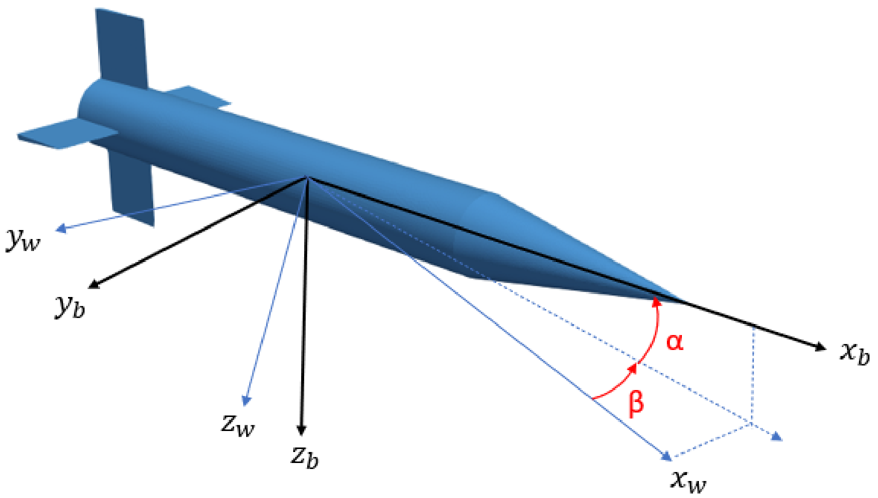

Figure 2.3: Representation of body frame and wind frame.

From equation (2.17), by assuming a zero sideslip angle, the following relations are obtained.

$$\begin{aligned} \omega_y = \Delta\dot{\alpha} = \dot{\theta}_y \\ \omega_z = -\Delta\dot{\beta} = -\dot{\theta}_x \sin\alpha + \dot{\theta}_z \cos\alpha \end{aligned} \tag{2.18}$$

Integrating equation (2.18) yields;

$$\begin{aligned} \Delta\alpha = \theta_y \\ \Delta\beta = \theta_x \sin\alpha - \theta_z \cos\alpha \end{aligned} \tag{2.19}$$

By substituting equation (2.18) and equation (2.19) into equation (2.15), the following relationship is obtained.

$$\begin{aligned} C_j = C_{j0} &+ \frac{\partial C_j}{\partial \beta} \sin\alpha_0 \theta_x + \frac{\partial C_j}{\partial \alpha} \theta_y - \frac{\partial C_j}{\partial \beta} \cos\alpha_0 \theta_z \\ &+ \left(\frac{\partial C_j}{\partial p} + \frac{\partial C_j}{\partial \dot{\beta}} \sin\alpha_0 \right) \dot{\theta}_x + \left(\frac{\partial C_j}{\partial q} + \frac{\partial C_j}{\partial \dot{\alpha}} \right) \dot{\theta}_y + \left(\frac{\partial C_j}{\partial r} - \frac{\partial C_j}{\partial \dot{\beta}} \cos\alpha_0 \right) \dot{\theta}_z \end{aligned} \tag{2.20}$$

By applying single degree of freedom motion in unsteady CFD analysis and wind tunnel tests, the stability derivatives can be extracted from equation (2.20) [1].

Applying rotation about the x axis of body frame with $\theta_y = \theta_z = \dot{\theta}_y = \dot{\theta}_z = 0$, equation (2.20) becomes;

$$C_j = C_{j0} + \frac{\partial C_j}{\partial \beta} \sin\alpha_0 \theta_x + \left(\frac{\partial C_j}{\partial p} + \frac{\partial C_j}{\partial \dot{\beta}} \sin\alpha_0 \right) \dot{\theta}_x \tag{2.21}$$

Applying rotation about the y axis of body frame with $\theta_x = \theta_z = \dot{\theta}_x = \dot{\theta}_z = 0$, equation (2.20) becomes;

$$C_j = C_{j0} + \frac{\partial C_j}{\partial \alpha} \theta_y + \left(\frac{\partial C_j}{\partial q} + \frac{\partial C_j}{\partial \dot{\alpha}} \right) \dot{\theta}_y \tag{2.22}$$

Applying rotation about the z axis of body frame with $\theta_x = \theta_y = \dot{\theta}_x = \dot{\theta}_y = 0$, equation (2.20) becomes;

$$C_j = C_{j0} - \frac{\partial C_j}{\partial \beta} \cos\alpha_0 \theta_z + \left(\frac{\partial C_j}{\partial r} - \frac{\partial C_j}{\partial \dot{\beta}} \cos\alpha_0 \right) \dot{\theta}_z \tag{2.23}$$

By using equations (2.21), (2.22) and (2.23), direct derivatives and cross derivatives can be calculated by implementing least square methods [1]. Some important aerodynamic moment derivatives are represented in Table 2.1.

Table 2.1: Stability derivative examples [1]

Motion	**Direct Derivatives**	**Cross Derivatives**
Rolling about x	$C_{l_\beta}, C_{l_p} + C_{l\dot{\beta}} \sin\alpha$	$C_{m_p} + C_{m\dot{\beta}} \sin\alpha, C_{n_p} + C_{n\dot{\beta}} \sin\alpha$
Pitching about y	$C_{m_\alpha}, C_{m_q} + C_{m\dot{\alpha}}$	$C_{l_q} + C_{l\dot{\alpha}}, C_{n_q} + C_{n\dot{\alpha}}$
Yawing about z	$C_{n_\beta}, C_{n_r} - C_{n\dot{\beta}} \cos\alpha$	$C_{l_r} - C_{l\dot{\beta}} \cos\alpha, C_{m_r} - C_{m\dot{\beta}} \cos\alpha$

Aerodynamic damping derivatives can be nondimensionalized by using the following relation.

$$C_{j\phi} = \frac{2V}{d} \frac{\partial C_j}{\partial \phi} \tag{2.24}$$

where ϕ represents the angular velocities of p, q, r, $\dot{\alpha}$ and $\dot{\beta}$. V is the freestream velocity and d is the reference length, which is equal to diameter of projectile.

The stability derivatives can be divided into static stability derivatives and dynamic stability derivatives. Aerodynamic derivatives, like C_{m_α}, C_{N_α}, C_{Y_β}, C_{n_β}, C_{A_u}, depending on steady flight conditions such as angle of attack, speed and sideslip angle can be called static stability derivatives while derivatives like C_{m_q}, $C_{m_{\dot{\alpha}}}$, C_{N_q}, C_{l_p} depend on the rates of the flight conditions can be named as dynamic stability derivatives or damping derivatives.

2.6.1 Prediction of Static Stability Derivatives

Static stability derivatives can be determined by using steady state CFD simulations. The main static stability derivatives used in flight mechanics and control studies can be summarized as; C_{A_u}, C_{N_u}, C_{m_u}, C_{A_α}, C_{N_α}, C_{m_α}, C_{Y_β}, C_{l_β} and C_{n_β}. In order to calculate the static stability derivatives, the central difference method given below can be used as follow;

$$C_j = \frac{C_{j_{(s_0+\Delta s)}} - C_{j_{(s_0-\Delta s)}}}{2\Delta s} \tag{2.25}$$

where $j = A, Y, N, l, m, n$ and $s = \alpha, \beta, u$. α and β represent angle of attack and sideslip angle. u defines the flight speed. s_0 is the mean value of the relevant flight condition. Δs is the perturbation about the mean value.

Also, static stability derivatives can be computed from the equations (2.21), (2.22) and (2.23) using the least square methods in unsteady calculations which will be discussed in the next section.

2.6.2 Prediction of Dynamic Stability Derivatives

Dynamic stability derivatives can be estimated by imposing rotational or translational motions around the aircraft center of gravity. In order to simulate these motions in SU2, 3D time dependent unsteady Reynolds-Averaged Navier-Stokes equations are solved. The unsteady flow analyzes are carried out by starting from the previously obtained steady state flow analysis results. After aerodynamic force and moment history obtained from the unsteady analyzes, dynamic stability derivatives can be calculated.

2.6.3 Unsteady Roll Analysis

2.6.3.1 Constant Roll Rate Analysis

The unsteady analysis using rigid mesh motion is performed under constant roll rate in order to obtain roll damping coefficient. When angle of attack is assumed to be zero, equation (2.21) becomes;

$$C_l = C_{l0} + C_{lp}\frac{pd}{2V} \tag{2.26}$$

C_{l0} in equation (2.26) is obtained from the steady state CFD calculations. To calculate C_{lp}, the following equation is used.

$$C_{lp} = \frac{C_l - C_{l0}}{pd/2V} \tag{2.27}$$

Also, this constant roll rate analysis can be solved in a steady manner by applying rotating frame. After computing the roll moment coefficient from the time independent steady state analysis under constant roll rate, the roll damping stability derivative can be calculated by using the same equation (2.27).

2.6.3.2 Sinusoidal Oscillating Motion Analysis

Sinusoidal oscillating motion can be used to predict aerodynamic stability coefficients. This motion can be described as;

$$\theta_x = \phi_A sin(\omega t) \tag{2.28}$$

where ϕ_A is the amplitude of the sinusoidal motion and ω is the rolling angular velocity. Taking time derivative of equation (2.28) yields;

$$\dot{\theta}_x = \phi_A \omega cos(\omega t) \tag{2.29}$$

Substituting equations (2.28) and (2.29) into equation (2.21), the following relation can be written for roll moment calculation.

$$C_l = C_{l0} + C_{l\beta} \sin\alpha_0 \phi_A sin(\omega t) + (C_{lp} + C_{l\dot{\beta}} \sin\alpha_0) \frac{\phi_A \omega cos(\omega t) d}{2V} \tag{2.30}$$

C_{l0}, C_{l_β} and $C_{lp} + C_{l\dot{\beta}} sin\alpha_0$ coefficients can be calculated from equation (2.30) by applying the least squares method. Also, if equation (2.21) is written for pitch and yaw moment calculations, the cross derivatives, $C_{m_p} + C_{m\dot{\beta}} \sin\alpha, C_{n_p} + C_{n\dot{\beta}} \sin\alpha$, can be computed similarly.

Least Squares Method

The least squares method [25] can be used to compute stability derivatives from the oscillating motion data [16]. Equation (2.30) has the same form as the equation given below.

$$y = a_0 + a_1 x_1 + a_2 x_2 + \ldots + a_p x_p + e \tag{2.31}$$

where $x_1, x_2, \ldots, x_p$ are the independent arguments, p is the number of independent variables, y is a dependent variable, $a_0, a_1, \ldots, a_P$ are unknown parameters and e is the approximation error. During the oscillating motion, roll angle, roll rate and aerodynamic coefficients are known. The n values of the instantaneous measurements of the p+1 variables are used to predict unknown parameters.

The linear regression model can be defined as;

$$\mathbf{y} = \mathbf{A}\mathbf{x} + \mathbf{e} \tag{2.32}$$

The unknown vector of the approximate solution is obtained by minimizing the functional $J = 1/2\|e\|^2$

$$\frac{\partial J}{\partial x_i} = 0, \qquad \text{for } i = 1, 2, \ldots, p \tag{2.33}$$

Consequently, $\left(\mathbf{A}^T\mathbf{A}\right)\mathbf{x} = \mathbf{A}^T\mathbf{y}$.

2.6.4 Unsteady Pitch Analysis

In this section, methods in order to predict pitch damping coefficients are explained.

2.6.4.1 Forced Oscillation Method

In order to compute pitch damping coefficient, air vehicle model is forced into a sinusoidal oscillation of small amplitude around the center of gravity. This motion can be defined as [7];

$$\alpha(t) = \alpha_0 + Asin(\omega t) \tag{2.34}$$

where α_0, A and ω are the mean angle of attack, the amplitude of pitching motion and the pitching angular velocity respectively.

The aerodynamic force and moment coefficients can be defined as follow;

$$C_j(t) = C_{j0} + C_{j\alpha}\alpha(t) + C_{jq}\frac{q(t)d}{2V} + C_{j\dot{\alpha}}\frac{\dot{\alpha}(t)d}{2V} \tag{2.35}$$

for $j = N, m$.

As stated before in equation (2.18), the rate of pitching motion and the rate of angle of attack are equal to each other, $q = \dot{\alpha}$. The forced oscillation motion is presented in Figure 2.4.

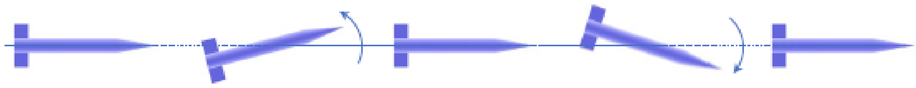

Figure 2.4: Sinusoidal forced oscillation, $q = \dot{\alpha}$ [6].

From equation (2.34), the following relation can be obtained.

$$q = \dot{\alpha} = A\omega cos(\omega t) \tag{2.36}$$

Bhagwandin and Sahu [7] use two different approaches in order to extract $C_{j_q} + C_{j_{\dot{\alpha}}}$ stability derivatives from equation (2.35).

<u>Integrating over a Period of Oscillation</u>

By implementing equation (2.34) and (2.36) into equation (2.35), and integrating equation (2.35) with respect to angle of attack, it yields the following equation [7].

$$C_{jq} + C_{j\dot{\alpha}} = \frac{2V}{d} \frac{\int \left[C_j(t) - C_{j0} - C_{j\alpha}\alpha(t)\right] \mathrm{d}\alpha}{\int \dot{a}(t) d\alpha} \tag{2.37}$$

Over one period of motion, the integrals of C_{j0} and $C_{j\alpha}$ are equal to zero. Then, equation (2.37) by changing the integral variable from the angle of attack to time can be rewritten as;

$$C_{j_q} + C_{j_{\dot{\alpha}}} = \frac{2V}{\pi d A} \int_0^T C_j(t) \cos\left(\frac{2Vk}{d} t\right) \mathrm{dt}, \quad j = N, m \tag{2.38}$$

where $T = 2\pi/\omega$ is the period of one cycle, and k is defined as reduced frequency which is equal to $k = \omega d/(2V)$.

$C_j(t)$ is obtained from the unsteady RANS calculations. The integral in equation

(2.38) can be calculated by applying trapezoidal rule as follow [7];

$$C_{j_q} + C_{j_{\dot{\alpha}}} = \frac{V}{\pi d A} \sum_{n=1}^{N_c} [t_{n+1} - t_n] \left[C_j(t) \cos\left(\frac{2Vk}{d} t \right) \right], \quad j = N, m \tag{2.39}$$

where N_c is the number of time steps to define one period of motion.

Solving at the Mean Angular Displacement Position

Another approach used by Bhagwandin and Sahu [7] is described in this section. This method is based on the relationship between pitch damping coefficient and angle of attack. An example of pitch moment coefficient history with respect to angle of attack obtained from force oscillation motion is represented in Figure 2.5.

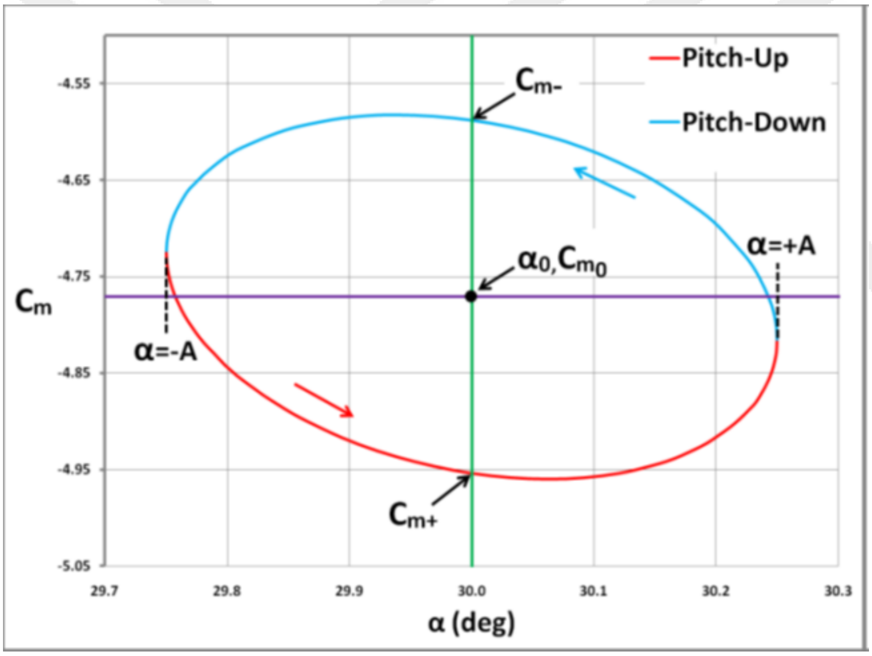

Figure 2.5: Example of pitching moment history with respect to angle of attack [7].

Considering the equation of $\alpha(t) = \alpha_0 + Asin(\omega t)$, $\alpha = \alpha_0$ is satisfied by using the following relation;

$$\mathrm{t}_{\alpha=\alpha_0} = \frac{\mathrm{n}\pi}{\omega} \quad \mathrm{n} = 0, 1, 2, 3, \ldots \tag{2.40}$$

where n represents every half cycle since α becomes equal to α_0 twice in every cycle during the pitch-up and pitch-down motions as shown in Figure 2.5.

Also, using the relation of $\dot{\alpha} = A\omega cos(\omega t)$ and equation (2.40), the following equation is derived at $\alpha = \alpha_0$.

$$\dot{\alpha}_{\alpha=\alpha_0} = (-1)^{\mathrm{n}}\omega\mathrm{A}, \quad \mathrm{n} = 0, 1, 2, 3, \dots \tag{2.41}$$

By using equations (2.35), (2.36) and (2.41), pitch damping derivative coefficient at the mean angle of attack can be calculated as;

$$\left[C_{j_q} + C_{j_{\dot{\alpha}}}\right]_{\alpha=\alpha_0} = (-1)^n \frac{(C_{j\pm} - C_{j_0} - C_{j_\alpha}\alpha_0)}{kA}, \quad n = 0, 1, 2, 3, \dots \tag{2.42}$$

Due to the symmetrical behavior of the pitch up and down motions, equation (2.42) can be simplified as;

$$\left[C_{m_q} + C_{m_{it}}\right]_{\alpha_0} = \frac{C_{m+} - C_{m-}}{2kA} \tag{2.43}$$

Least Squares Method

An alternative approach to determine pitch damping derivative is the least squares method, similar to unsteady roll calculations. During the forced oscillation motion, angle of attack, angle of attack rate, pitching angular velocity and aerodynamic coefficients are known. By using the least squares method explained in above section, pitch damping derivatives can be computed.

2.6.4.2 Differential Method

This method estimates pitch damping derivatives by forcing the aircraft to move to the same angle of attack with different angular velocities [8] as represented in Figure 2.6.

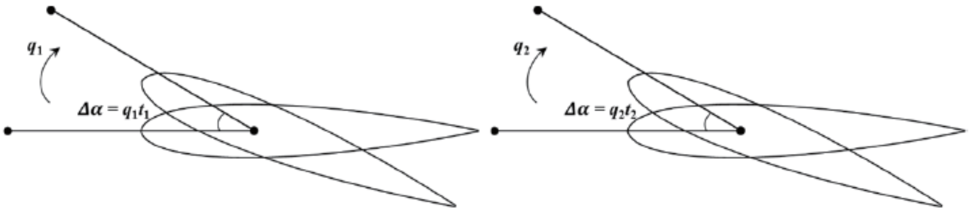

(a) Rotating to $\Delta\alpha$ with q_1 (b) Rotating to $\Delta\alpha$ with q_2

Figure 2.6: Differential method, rotating to the same angle of attack with different pitching angular velocity [8]

$$\Delta\alpha = q_1 t_1 = q_2 t_2 \tag{2.44}$$

By using equation (2.35) and $q = \Delta\dot{\alpha}$, the following relations are obtained.

$$C_{m1} = C_{m0} + C_{ma}\Delta\alpha + \left(C_{m\dot{\alpha}} + C_{mq}\right)\bar{q}_1 \tag{2.45}$$

$$C_{m2} = C_{m0} + C_{m\alpha}\Delta\alpha + \left(C_{m\dot{\alpha}} + C_{mq}\right)\bar{q}_2 \tag{2.46}$$

After subtracting equation (2.46) from equation (2.45), the pitch damping derivative of $C_{m\dot{\alpha}} + C_{mq}$ can be calculated as follows;

$$C_{m\dot{\alpha}} + C_{mq} = \frac{C_{m1} - C_{m2}}{\bar{q}_1 - \bar{q}_2} \tag{2.47}$$

where $\bar{q}_1 = q_1 d/(2V)$ and $\bar{q}_2 = q_2 d/(2V)$.

2.6.4.3 Plunging Oscillation Method

This method can be used to determine the single translational dynamic derivatives of $C_{m\dot{\alpha}}$ and $C_{N\dot{\alpha}}$ by applying a small plunging oscillation. This motion is formulated as

[17];

$$\boldsymbol{z}(t) = \boldsymbol{z}_m \sin(\omega t) \tag{2.48}$$

where z_m is the plunging amplitude and ω is the plunging angular velocity.

The unsteady pitching force and moment formulation during the plunging motion is given as;

$$C_j(t) = C_{j0} + C_{j\alpha}\alpha(t) + C_{j\dot{\alpha}}\frac{\dot{\alpha}(t)d}{2V}, \quad j = N, m \tag{2.49}$$

Taking derivatives of equation (2.48) with respect to time gives the following equations.

$$v_z = \dot{z}(t) = \omega z_m \cos(\omega t) \tag{2.50}$$

$$\dot{v}_z = \ddot{z}(t) = -\omega^2 z_m \sin(\omega t) \tag{2.51}$$

Then, α and $\dot{\alpha}$ can be calculated by using the following relations.

$$\begin{aligned} \alpha &= \frac{\omega z_m \cos(\omega t)}{V} \\ \dot{\alpha} &= \frac{-\omega^2 z_m \sin(\omega t)}{V} \end{aligned} \tag{2.52}$$

where α is the angle of attack due to plunge motion and $\dot{\alpha}$ is the angle of attack rate. In this study, the mean angle of attack value is assumed to be zero. The pure plunging motion is represented in Figure 2.7.

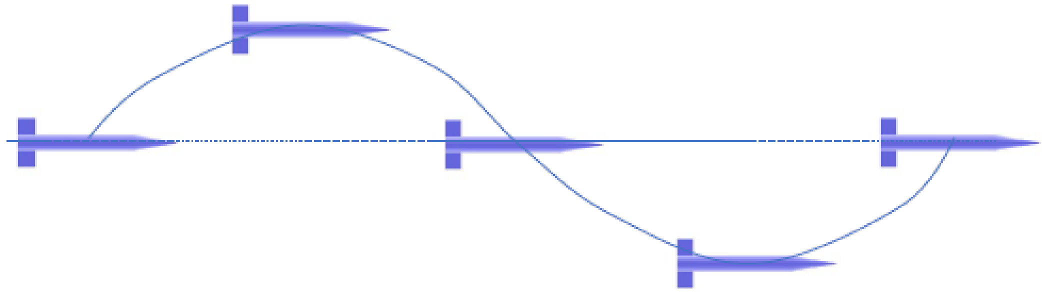

Figure 2.7: Pure plunging motion, $q = 0$ and $\dot{\alpha} = sin(\omega t)$ [6].

Inserting equation (2.52) into equation (2.49) leads to the following relation.

$$C_j = C_{j0} + C_{j\alpha}\frac{\omega z_m \cos(\omega t)}{V} + C_{j\dot{\alpha}}\frac{-\omega^2 z_m \sin(\omega t) d}{2V^2}, \quad j = N, m \tag{2.53}$$

When $\omega t = 2n\pi + \pi/2$, $C_{j\dot{\alpha}}$ can be solved as;

$$C_{j\dot{\alpha}} = \frac{C_j - C_{j0}}{-k\omega z_m/V}, \quad j = N, m \tag{2.54}$$

Also, the aerodynamic coefficient of $C_{j\dot{\alpha}}$ can be computed by using the least squares method from the history of angle of attack, angle of attack rate and aerodynamic coefficients.

CHAPTER 3

VALIDATION

In this part of the thesis, validation of the numerical methodology is carried out. The basic finner reference projectile [2] model aformentioned is used to for this purpose since it has experimental data consisting of wind tunnel and free flight tests in the literature.

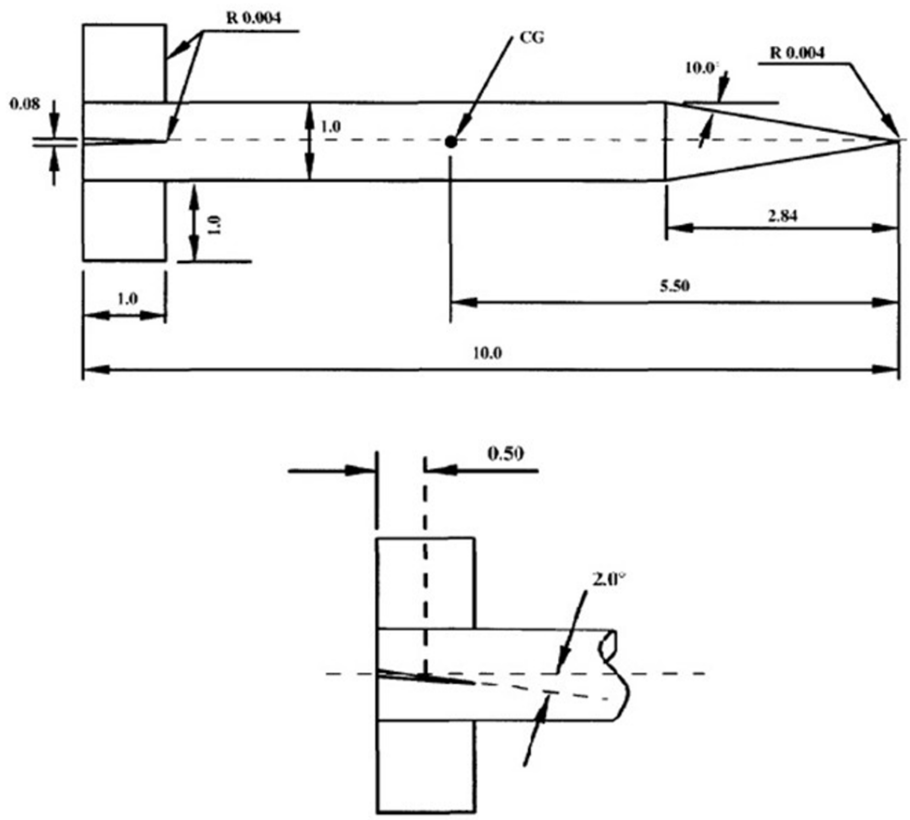

Figure 3.1: Basic finner geometry, dimensions in calibers, one caliber = 0.03 m [2].

The basic finner geometry is represented in Figure 3.1. It has 20 degree nose cone and four rectangular fins with 2 degrees of cant angle. The body length to diameter ratio is 10. The center of gravity of the projectile is taken at a distance of 5.5 caliber from the nose [2]. In order to nondimensionalize the aerodynamic force and moment coefficients, the reference area is chosen as the cross-sectional area at which the projectile diameter is maximum. Also, the maximum projectile diameter of the basic finner is used as the reference length.

3.1 Computational Domain and Boundary Conditions

Unstructured computational grids are constructed by using Pointwise® V18.3R1. A spherical farfield boundary of a radius of 200 calibers is formed as shown in Figure 3.2. The mesh density is increased in a cylindrical region around the body as shown in Figure 3.3 in order to accurately solve the flow physics near the body and wake region.

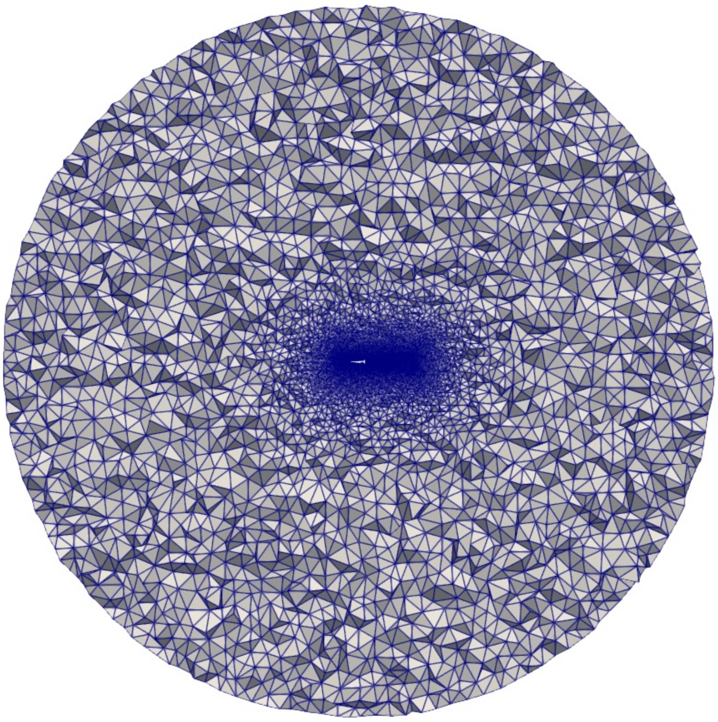

Figure 3.2: Spherical computational domain general view.

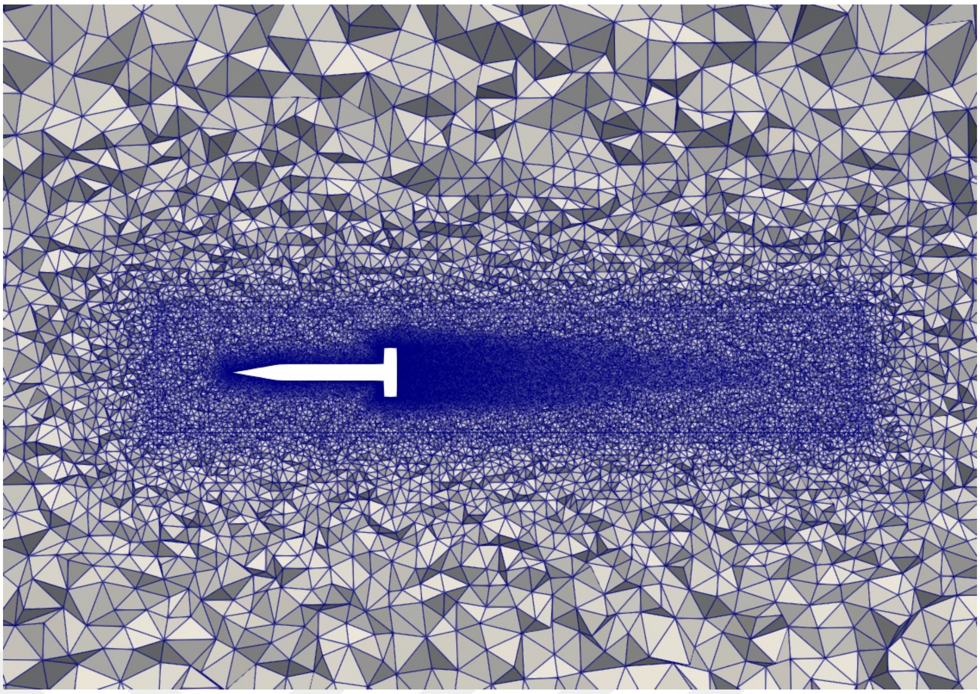

Figure 3.3: Refine cells near the body.

In order to successfully resolve the boundary layer over the model, a prism-based boundary layer mesh with 30 layers is generated. The first layer thickness is calculated to satisfy the $y+ \leq 1$ criteria for each Mach number. Figure 3.4 is presented to show the surface mesh and boundary layer mesh more closely.

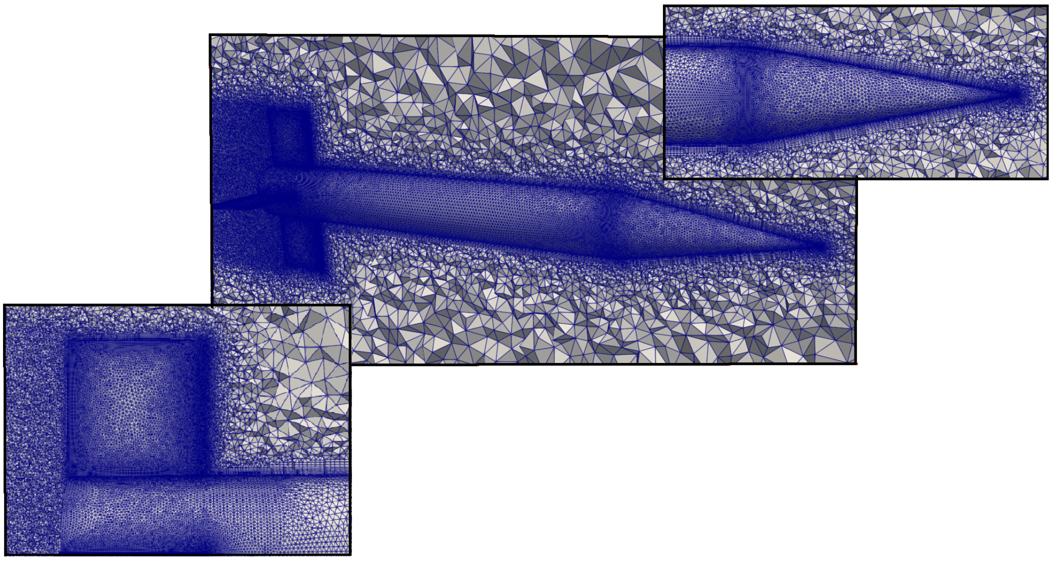

Figure 3.4: Surface and boundary layer mesh.

Adiabatic wall boundary condition is applied at the surface of the basic finner geometry, while far-field boundary condition is used on the outer computational domain boundary.

In this study, the same mesh is used for supersonic and subsonic velocities. The grid density is needed to be increased in the areas such as shock regions, flow separation points and in the base region where high pressure gradients are present. Therefore, a cylindrical fine mesh area is created around the body to solve supersonic flow correctly. As a result, a finer mesh is constructed than required for subsonic velocities.

3.2 Grid Convergence Study

In order to investigate the dependence of the results on the mesh density, aerodynamic coefficients are calculated first for four different mesh sizes of 8.1, 15.4, 22.7 and 29.8 million cells. The computed effects of the grid density on the axial force coefficient (C_A), normal force coefficient (C_N), pitching moment coefficient (C_m) and roll moment coefficient (C_l) for Mach 0.766 and Mach 1.832 are shown in Figure 3.5, Figure 3.6, Figure 3.7 and Figure 3.8, respectively. These results were obtained through RANS solutions using the Jameson-Schmidt-Turkel scheme and Spalart-Allmaras turbulence model. For both Mach numbers, when the mesh density is greater than 15.4 million cells, the change in aerodynamic coefficients does not exceed 1.5%. It is observed that the change in the coefficients of C_N, C_m and C_l is even less than 1.0%. The grid of 15.4 million cells provides sufficient accuracy according to the grid dependency study. Also, the increase in mesh size increases the computational cost. Therefore, the grid of 15.4 million cells is selected for the CFD analysis to be carried out within the scope of this thesis.

"ber."

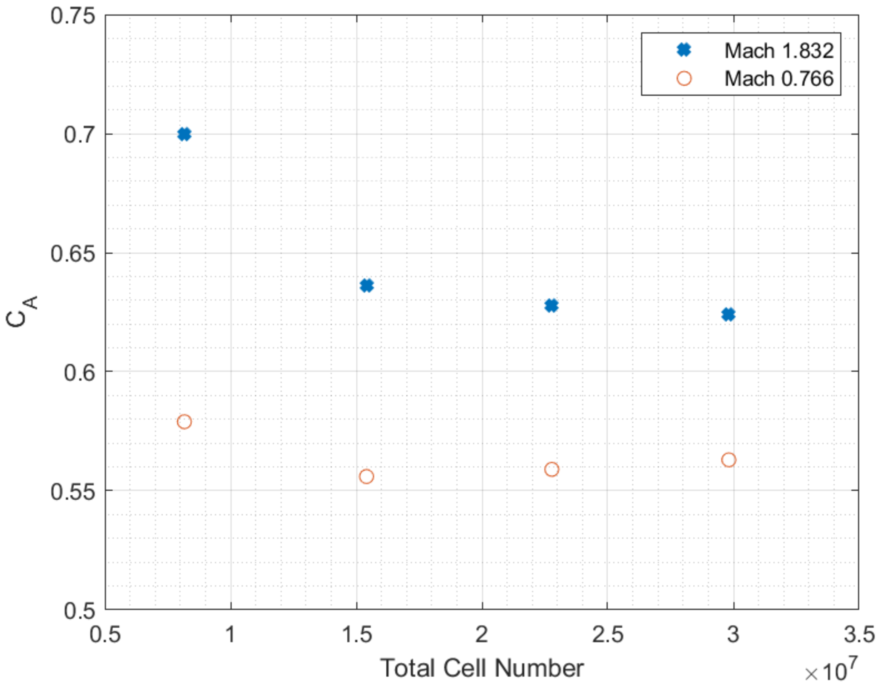

Figure 3.5: Axial force coefficient with respect to the total cell number.

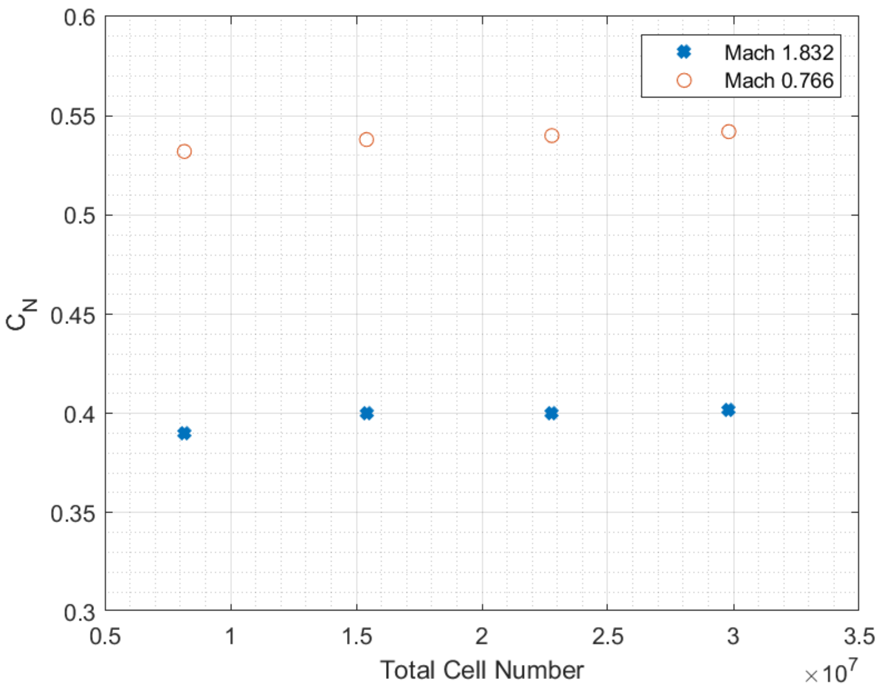

Figure 3.6: Normal force coefficient at 2° angle of attack according to total cell number.

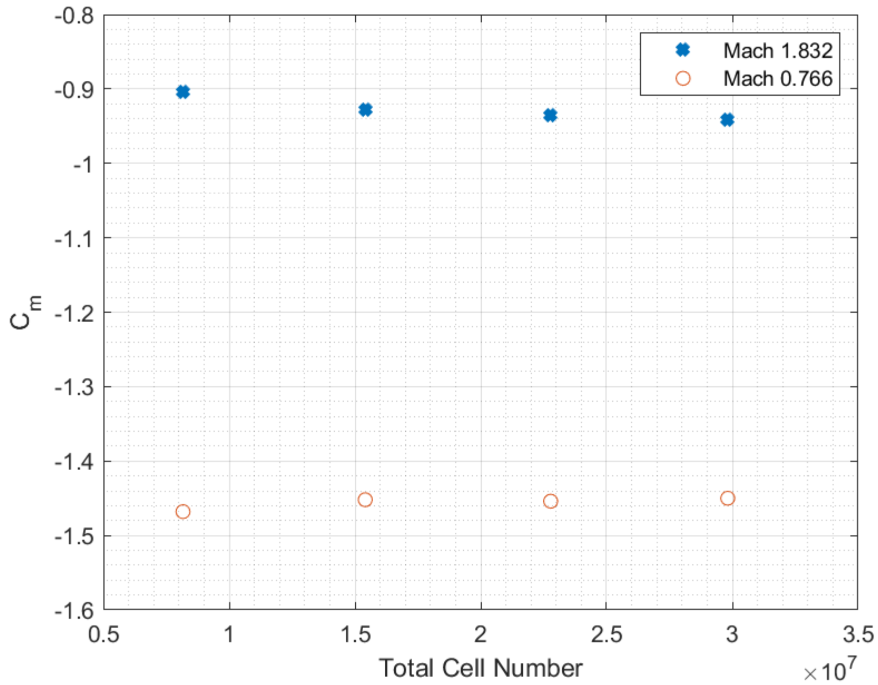

Figure 3.7: Pitching moment coefficient at 2° angle of attack according to total cell number.

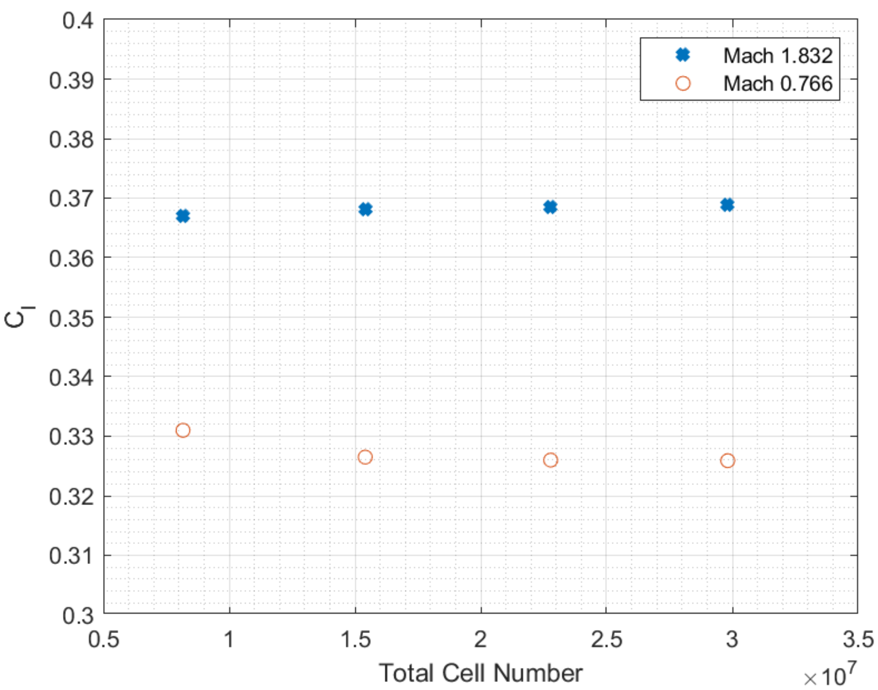

Figure 3.8: Roll moment coefficient according to the total cell number.

3.3 Comparison of Numerical Results and Experimental Results

In reference [2], there are aerodynamic stability derivatives for the basic finner projectile obtained from free flight and wind tunnel tests. In order to assess the accuracy of the numerical method used with the constructed mesh size of 15.4 million cells, SU2 results are compared with the experimental data. Also, in order to examine the effect of turbulence models on aerodynamic coefficients, both SA and SST models are used in CFD calculations. In this section, comparisons are made for the axial and normal force coefficients. Also, the dynamic derivatives calculated with SU2 are compared with the free flight experimental data in the later part of this study. Since the dynamic derivatives are obtained only by free flight tests in reference [2], CFD analyzes are carried out by using the same flight conditions as the free flight tests. The wind tunnel and free flight Reynolds numbers with respect to Mach numbers are given in Table 3.1.

Table 3.1: Reynolds Numbers of wind tunnel and free flight experiments [2].

Mach	**Wind Tunnel Re**	**Free Flight Re**
0.5	2.90E+06	3.40E+06
0.6	3.20E+06	4.10E+06
0.7	3.60E+06	4.80E+06
0.8	3.90E+06	5.50E+06
0.92	4.20E+06	6.30E+06
1	4.30E+06	6.90E+06
1.15	4.20E+06	7.90E+06
1.28	4.40E+06	8.80E+06
1.38	4.20E+06	9.50E+06
1.5	4.60E+06	1.03E+07
1.75	4.20E+06	1.20E+07
2	3.80E+06	1.37E+07

The comparison of axial force coefficients is presented in Figure 3.9. The same Reynolds numbers as those of the free flight tests are used in the CFD computations.

Since the axial force coefficient is highly depend on Reynolds number, the coefficient obtained from the wind tunnel tests are not represented in Figure 3.9. In this figure, FF means the free flight data. Also, MF and SF represents the data obtained from multiple fit and single fit data reduction techniques respectively. The data reduction system is based on assembling the dynamic data such as time, position and angles, and performing linear theory and six degree of freedom analyzes to estimate aerodynamic coefficients. The six degree of freedom analyzes include the Maximum Likelihood Method in order to match experimental and theoretical trajectories. This data reduction system fit multiple data sets in order to obtain a more accurate aerodynamic data [2].

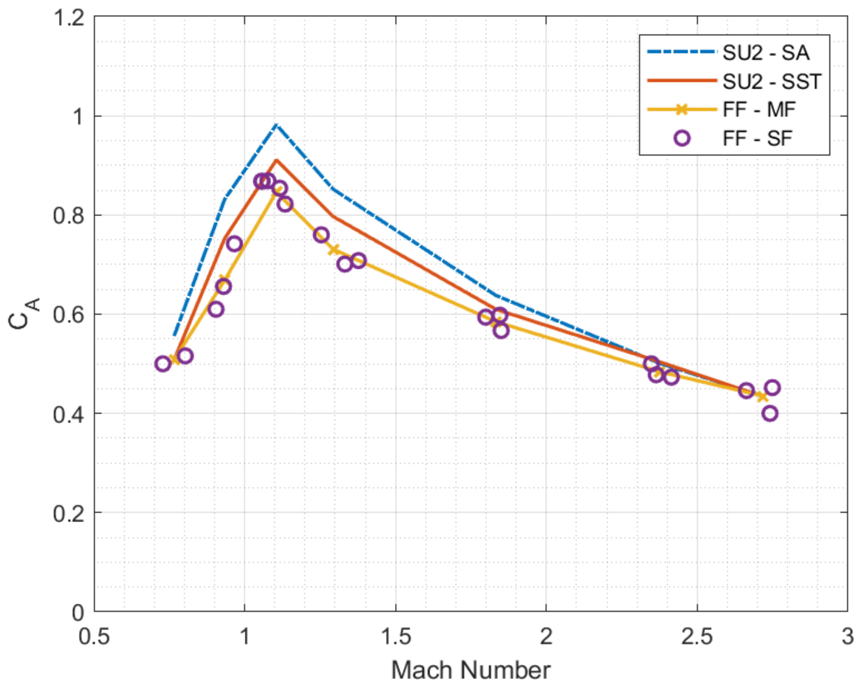

Figure 3.9: Axial force coefficient with respect to Mach number.

From Figure 3.9, it is seen that the results of the analysis made with the SST turbulence model are closer to the experimental data. When the pressure distribution calculated with two turbulence models are examined, it is seen that the highest pressure difference occurs at the wake region of the projectile where the turbulent flow is dominant. At high supersonic speeds, there is no significant difference between the CFD solutions and experimental data. However, it is investigated that the SA turbulence model overestimates the axial force coefficient in subsonic and transonic regimes. Also, the difference between the experimental data and CFD solutions are larger in transonic regime due to complicated flow phenomena.

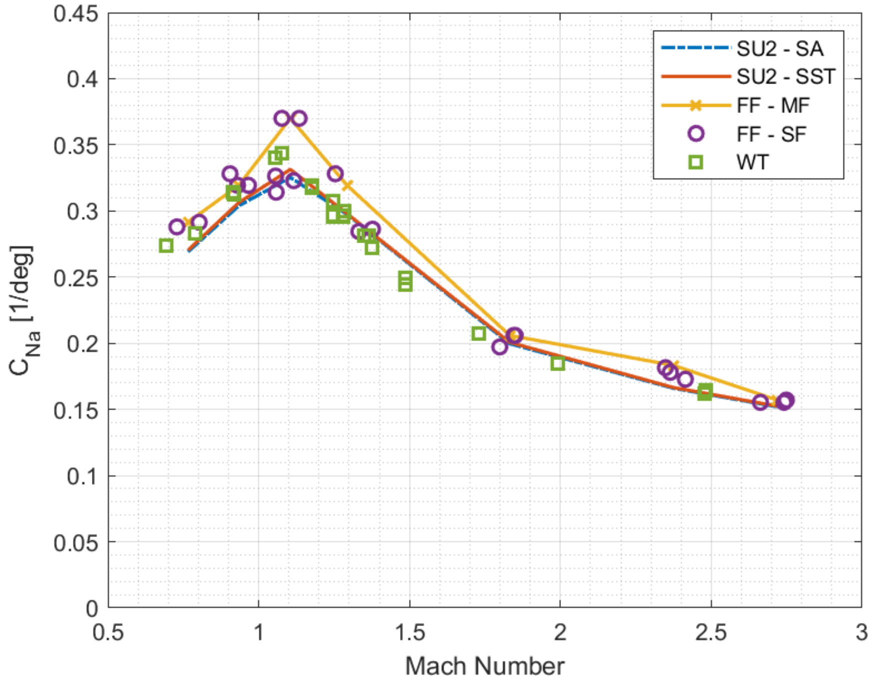

Figure 3.10: $C_{N\alpha}$ with respect to Mach number.

The normal force coefficient derivatives with respect to the angle of attack computed by CFD and measured data are compared in Figure 3.10. Since the normal force coefficient is not much affected by the Reynolds number in the linear regime at low angles of attack, the wind tunnel test results are also taken into account in this comparison. When Figure 3.10 is examined, the CFD results show good agreement with the wind tunnel data and free flight data. In addition, it is observed that the results of CFD analysis performed with both turbulent models are close to each other. The biggest difference between the CFD and experimental data is seen in transonic regime.

The fin geometry used in this study has 2 degree cant angle which produces roll moment. The roll moment derivatives with respect to cant angle (δ) are calculated by using CFD. The results are compared with the experimental data as shown in Figure 3.11.

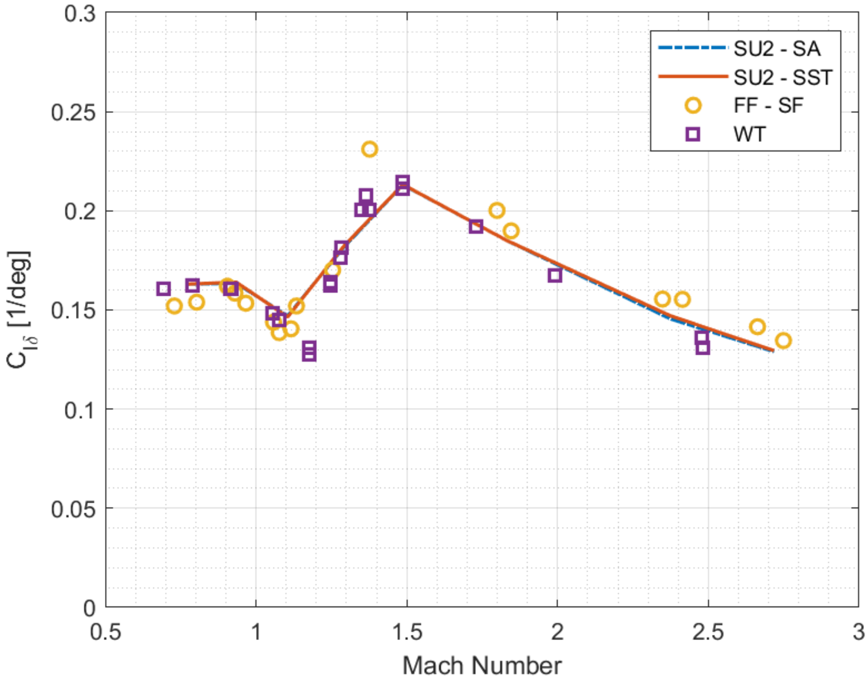

Figure 3.11: $C_{l\delta}$ with respect to Mach number.

Figure 3.9, 3.10 and 3.11 show that CFD calculations generally show good agreement with experimental data especially in subsonic and high supersonic regimes.

CHAPTER 4

RESULTS AND DISCUSSION

In this chapter, the prediction of stability derivatives by using the SU2 code is presented. Firstly, the results of steady state computations are introduced. Then, unsteady roll and pitch dynamics calculations are given. The effects of the turbulence model are investigated for steady and unsteady analyzes. The dynamic stability derivative solutions obtained using the different methods described in Chapter 2 are presented.

4.1 Steady State Analysis Results

In this section, the results of the steady state calculations are presented. All steady SU2 analyzes are carried out using RANS equations. The Courant-Friedrichs-Lewy (CFL) condition of the finest grid is chosen as 0.5, initially. Automatic CFL adaption that allows the CFL number to be increased gradually to higher values is used. The minimum and maximum bounds of the allowable CFL number are selected as 0.1 to 25.

The first layer thickness is calculated based on the maximum Mach number used in this study to satisfy the criteria $y+ \leq 1$. Therefore, the initial Δs is calculated as $4e-7\ m$. The $y+$ distribution on the surface for Mach 2.718 is represented in Figure 4.1.

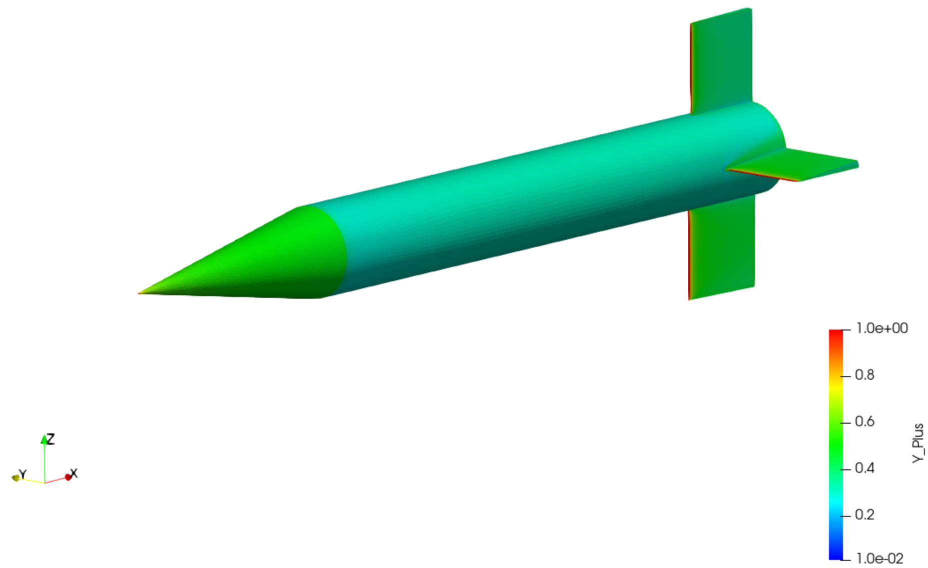

Figure 4.1: $y+$ for 2.718 Mach.

As it can be seen from the figure above, the $y+$ on the surface is less than 1. However, at the leading edge of the basic finner projectile fins, the value of y^+ is just above 1.

One of the aims of this thesis is to compare the dynamic derivatives calculated using different methods. Thus, the comparisons will be performed by considering two main Mach numbers of 0.766 and 1.832. For this reason, steady calculations of these Mach numbers at zero angle of attack are emphasized and Mach contours on the symmetry plane are presented in Figure 4.2 and Figure 4.3 in order to examine the flow fields. The figures show low velocity flow at the base of the projectiles. In addition, shock waves and expansion waves can be seen in the figures.

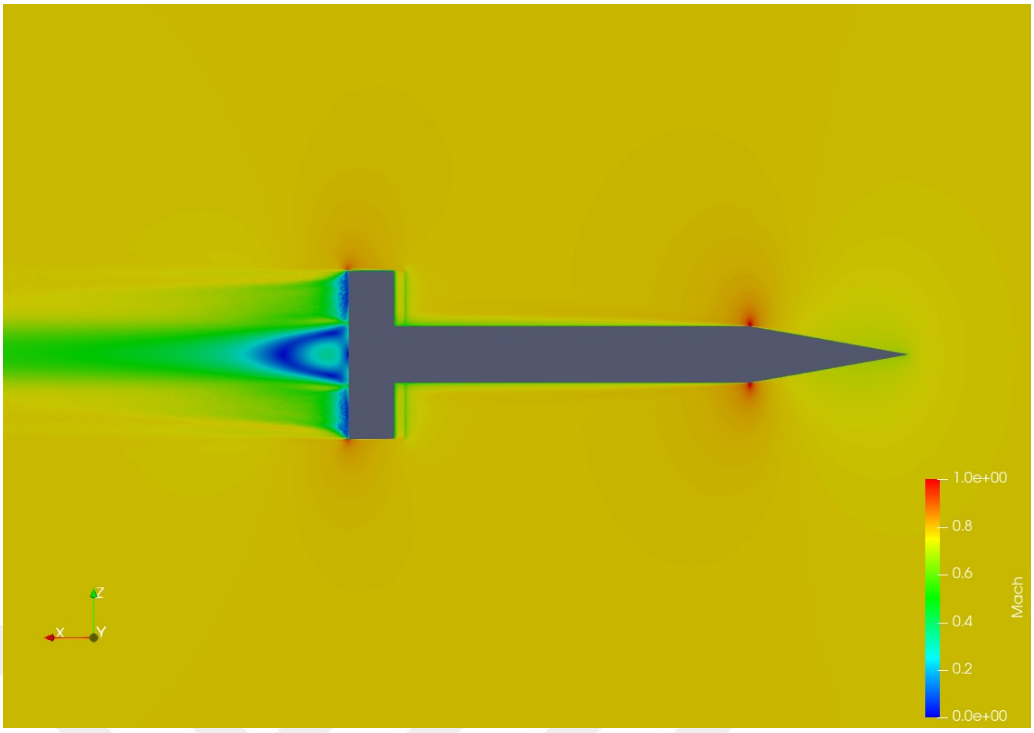

Figure 4.2: Mach number contour for Mach 0.766.

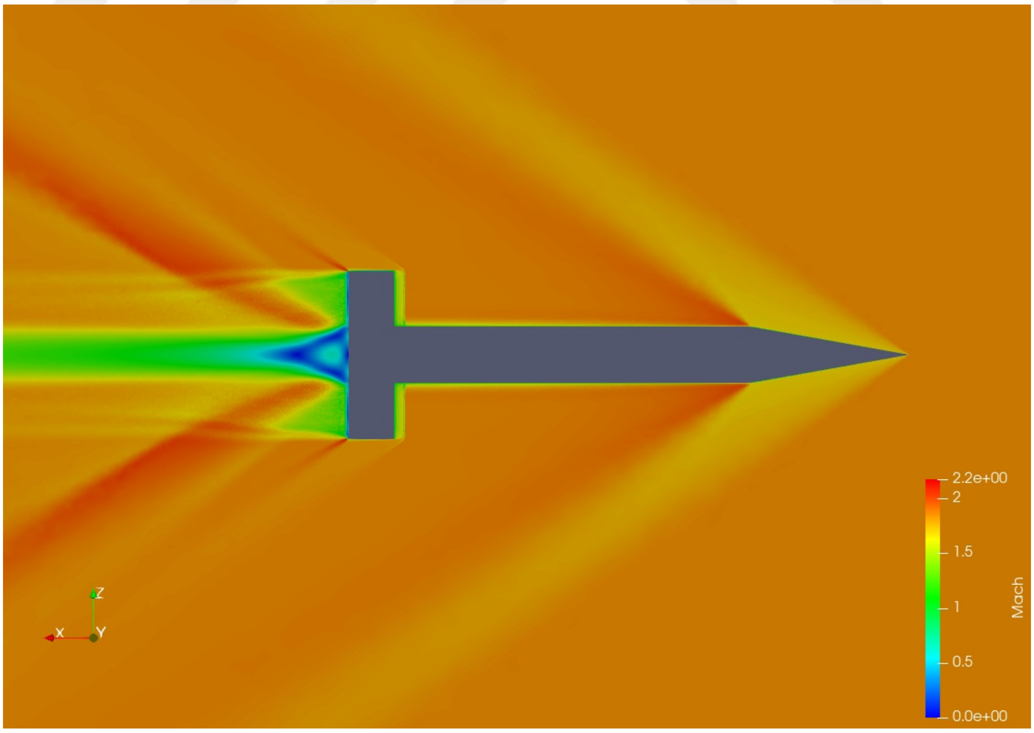

Figure 4.3: Mach number contour for Mach 1.832.

The static stability derivatives are calculated at zero mean angle of attack by using equation (2.25). The steady RANS computations are performed with different angles of attack to predict the longitudinal stability derivatives. Since the basic finner geometry is axisymmetric, the longitudinal stability derivatives can be taken equal to the lateral stability derivatives. Therefore, in this study, the longitudinal stability derivatives are usually considered.

The main longitudinal static stability derivatives are the normal force coefficient derivative with respect to angle of attack ($C_{N\alpha}$) and the pitching moment coefficient derivative with respect to angle of attack ($C_{m\alpha}$). These derivatives are calculated with steady state RANS computations at different Mach numbers. The calculated aerodynamic stability coefficients of $C_{N\alpha}$ were presented in Figure 3.10. The $C_{m\alpha}$ stability coefficients computed using SA and SST turbulence models are represented in Figure 4.4. In addition to the CFD solutions with different turbulence models, the available experimental data are also presented in Figure 4.4 for comparison.

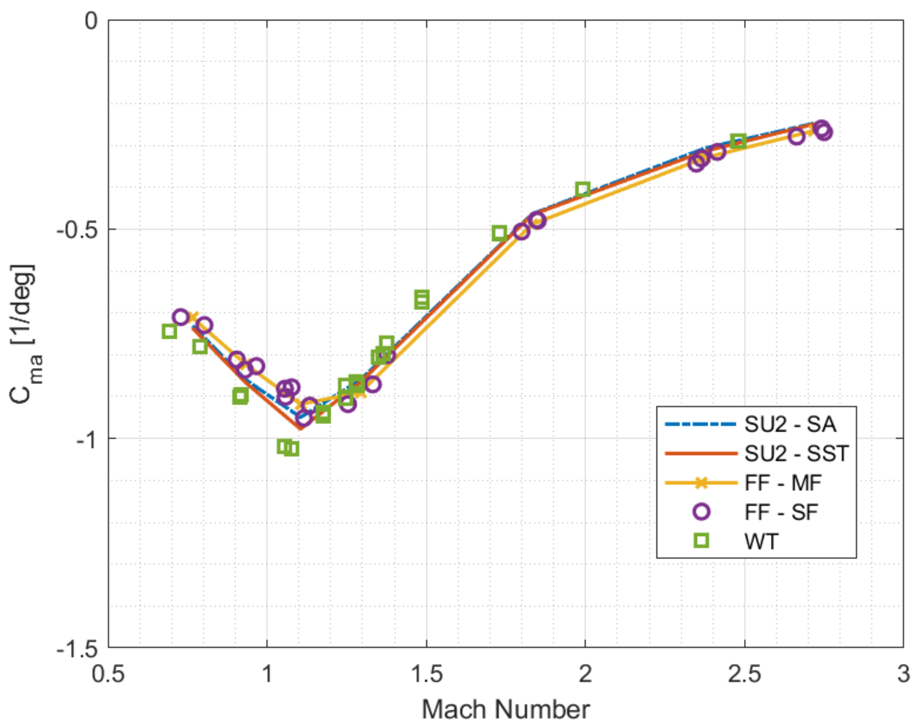

Figure 4.4: $C_{m\alpha}$ vs Mach number.

Figures 3.10 and 4.4 show that the longitudinal stability derivatives computed with

CFD agree well with the experimental data. Also, both Spalart-Allmaras and Shear-Stress-Transport turbulence models give similar results. In order to examine the computational cost of the analyzes carried out by the turbulence models, the analysis run times for the same number of iterations are recorded and presented in the table below. The analyzes are carried out with 20 Core Intel(R) Xeon(R) Gold 6148 CPU @2.4 Ghz.

Table 4.1: Solution times according to turbulence model

Turbulence Model	Solution Times [s]
Spalart-Allmaras (SA) Model	14796
Menter Shear Stress Transport (SST) Model	15954

Since the SA turbulence model solves one equation whereas the SST turbulence model solves two equations, the solution time of the SA model is shorter as expected. Due to the computational cost, the SA turbulence model is chosen to be used in the unsteady analyzes.

The comparison between the SA and SST turbulence models in terms of eddy viscosity in the flow field is demonstrated in Figure 4.5. The figure shows that the main difference in the flow field is occurred at the base of the projectile. This is the reason for the difference in the axial force coefficients obtained with different turbulence models.

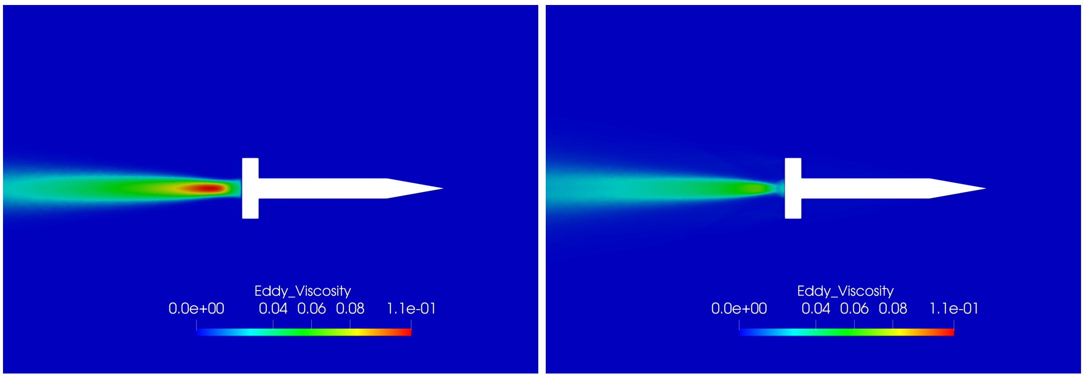

(a) SA turbulence model.

(b) SST turbulence model.

Figure 4.5: Comparison of SA and SST turbulence models.

4.2 Unsteady Roll Analysis

4.2.1 Constant Roll Rate Analysis

Roll damping coefficient is calculated by using unsteady RANS equations with rigid mesh motion under constant roll rate. For Mach 0.766 and Mach 1.832, unsteady RANS analyzes are performed with the SA turbulence model by using 25 inner iterations and time step is chosen as $\Delta t = 1e - 5\ s$. Also, the reduced frequency for these simulations is taken as $k = 0.05$ at the beginning of the constant roll rate analysis. The results obtained for different reduced frequencies and time steps will be presented on the following pages. The reduced frequency is defined as $k = pd/(2V)$ where p is the roll rate, d is the diameter of the basic finner and V is the freestream velocity. The convergence history of the unsteady computations under constant roll rate is demonstrated in Figure 4.6. As it can be seen from the figure, the rolling moment coefficients converge to a single value. It is seen that the number of iterations required for the convergence of the analysis in the supersonic case is lower.

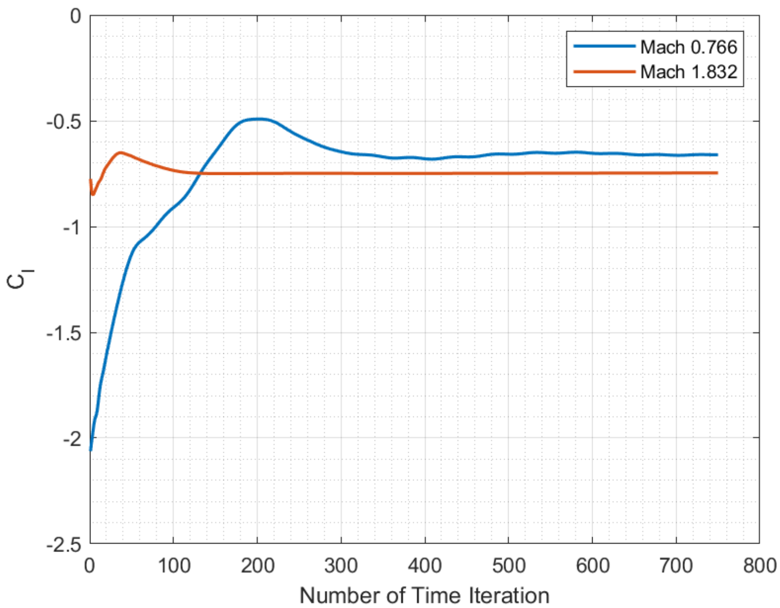

Figure 4.6: Convergence history of unsteady simulation under constant roll rate.

By using equation (2.27), the roll damping coefficients for both Mach numbers are calculated. C_{l_0} in this equation is obtained from the steady state analysis. The results are given in the following table. Also, the free flight experimental data are presented in the same table for comparison.

Table 4.2: Roll damping coefficients calculated with CFD and experiment.

Mach Number	**CFD Results**	**Free Flight Data**	**Relative Difference [%]**
0.766	-19.42	-17.6	10.4
1.832	-22.58	-22.4	1.0

As it can be seen from Table 4.2, the difference between CFD computation and free flight data is larger at subsonic speed. For this reason, the effect of basic simulation parameters such as time step and reduced frequency used in unsteady calculations on the solution is investigated. Firstly, time step is decreased to $\Delta t = 1e - 6\ s$ and the simulations are performed. The results of the CFD calculations for different time steps are presented in Table 4.3.

Table 4.3: CFD results of roll damping coefficients for different time steps ($k = 0.05$).

Mach Number	$\Delta t = 1e - 5\ s$	$\Delta t = 1e - 6\ s$
0.766	-19.42	-19.40
1.832	-22.58	-22.57

Table 4.3 shows that the roll damping coefficients are similar for both time steps. Moreover, the results of the CFD calculations with different reduced frequencies are indicated in Table 4.4

Table 4.4: CFD results of roll damping coefficients for different reduced frequencies.

Mach Number	$k = 0.01$	$k = 0.05$	$k = 0.1$
0.766	-18.80	-19.42	-21.07
1.832	-22.10	-22.58	-22.70

As it can be seen from the above table, changing reduced frequency in supersonic regime does not effect the roll damping coefficient significantly. However, when reduced frequency is decreased for unsteady computations of Mach 0.766, the roll damping coefficient approaches to the experimental data. This is because when the reduced frequency is lowered, the rolling speed becomes smaller; thus, the velocity contribution of the angular velocity on the cells is reduced. With high rotational velocity, when the Mach number is equal to 0.766, higher velocity occurs within the domain, which cause the flow to be closer to the transonic regime so deviations can be seen. Figure 4.7 shows that the Mach number contour on the $y - z$ plane that pass through the middle of the fins. As it can be seen from the figure, when reduced frequency is equal to $k = 0.05$, higher Mach numbers are observed in the flow domain than in the case of $k = 0.01$.

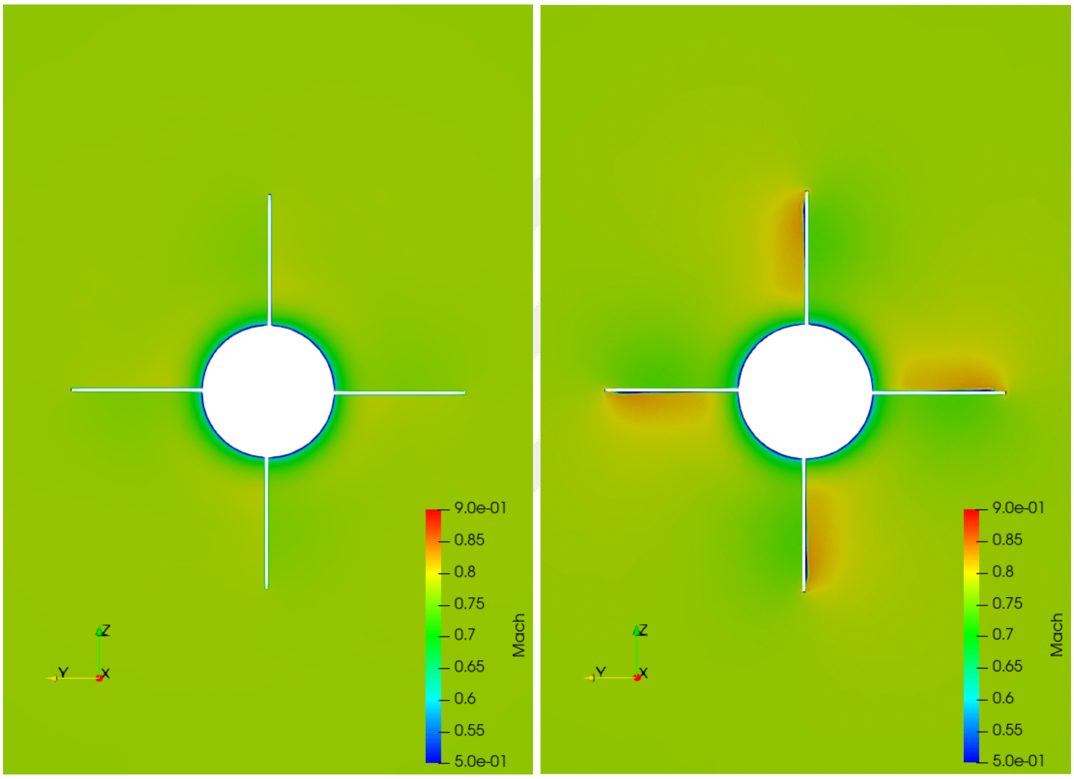

(a) Mach contour for $k = 0.01$.

(b) Mach contour for $k = 0.05$.

Figure 4.7: Mach number contour on $y - z$ plane at the middle of fins.

Turbulence models do not significantly affect the stability derivatives in steady state simulations. Now, their effects on the unsteady results are examined. The results obtained with SA and SST turbulence models are shown in the table below.

Table 4.5: Turbulence model effect on roll damping coefficient ($k = 0.05$).

Mach Number	**SA Model**	**SST Model**
0.766	-19.42	-19.49
1.832	-22.58	-22.57

The results show that there is no difference between turbulence models so that unsteady roll analysis can be performed using SA model due to cost effectiveness.

In addition to the rigid mesh motion option, rotating frame formulation in SU2 [24] is used to compute the roll damping coefficient. Therefore, CFD analyzes are carried out in a steady manner with the rotating frame option. The rotational angular velocity for the rotating frame is used with a reduced frequency of $k = 0.05$. The convergence history of the roll moment coefficients for both Mach numbers is demonstrated in Figure 4.8.

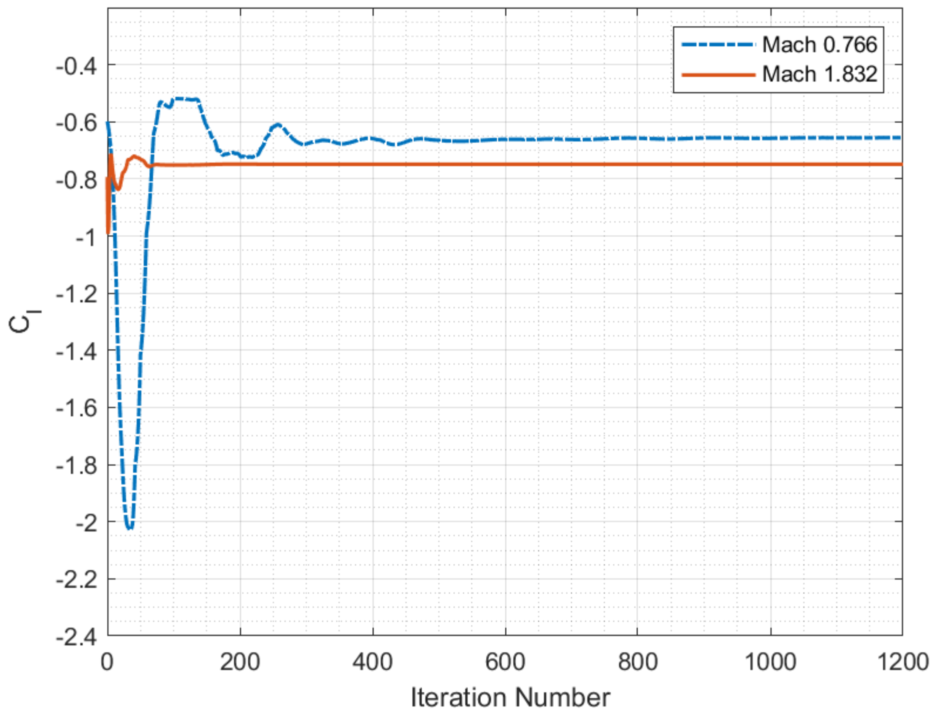

Figure 4.8: Convergence history of roll moment coefficients with rotating frame option.

As it can be seen from the above figure, when rotating frame option is used, the convergence of the low speed (Mach 0.766) case needs more iterations as in the unsteady calculations with rigid mesh motion. The rotating frame option allows faster convergence for constant roll rate analysis. The roll damping coefficients computed by using the rotating frame approach are compared in the following table.

Table 4.6: Comparison of rigid motion and rotating frame results ($k = 0.05$).

Mach Number	**Rigid Motion**	**Rotating Frame**
0.766	-19.42	-19.45
1.832	-22.58	-22.59

As it can be seen from Table (4.6), both methods of rigid motion and rotating frame give almost the same results. The advantage of the rotating frame under constant roll rate is the computational cost due to less costly computation of the steady state flow.

4.2.2 Sinusoidal Oscillating Motion Analysis

4.2.2.1 Prediction of Rolling Moment Coefficients

Sinusoidal oscillating motion can be used to calculate the roll damping coefficient. Unsteady analyzes are performed by applying sinusoidal motion about the x axis of body frame. This motion can be formulated as follows;

$$\theta_x = \phi_A sin(\omega t) \tag{4.1}$$

where ϕ_A is the amplitude of sinusoidal motion and ω is the rolling angular velocity.

The time derivative of equation (4.1) gives;

$$\dot{\theta}_x = \phi_A \omega cos(\omega t) \tag{4.2}$$

Equation (2.30) can be rewritten for aerodynamic static and dynamic roll coefficients as;

$$C_l = C_{l0} + \frac{\partial C_l}{\partial \beta} \sin\alpha_0 \theta_x + \left(\frac{\partial C_l}{\partial p} + \frac{\partial C_l}{\partial \dot{\beta}} \sin\alpha_0 \right) \dot{\theta}_x \tag{4.3}$$

Implementing equations (4.1) and (4.2) into (4.3), and assuming angle of attack is equal to zero ($\alpha_0 = 0$), the following relation is obtained.

$$C_l = C_{l0} + C_{lp} \frac{\phi_A \omega cos(\omega t) d}{2V} \tag{4.4}$$

The unsteady roll analysis is carried out with $\phi_A = 10°$ and $k = \omega d/(2V) = 0.05$. The variation of roll moment coefficient with roll angle during the sinusoidal oscillating motion with three periods is indicated in Figure 4.9 for both Mach numbers. The figure indicates that after some transition iterations, the solution becomes periodic.

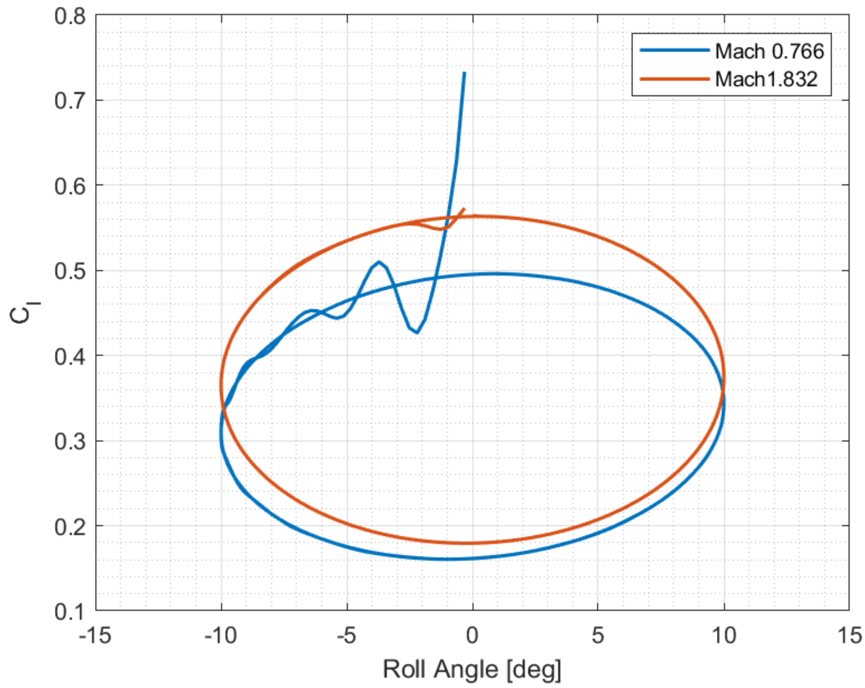

Figure 4.9: Variation of roll moment coefficient with roll angle.

By applying the least squares method with equation (4.4), C_{l0} and C_{lp} aerodynamic coefficients are calculated. They are given in Table 4.7. Also, the roll moment coefficients (C_{lp}^{FF} and C_{l0}^{FF}) of the free flight experiment are presented in the table.

Table 4.7: C_{l0} and C_{lp} coefficients at zero angle of attack

Mach Number	C_{l0}	C_{lp} $[1/rad]$	C_{l0}^{FF}	C_{lp}^{FF} $[1/rad]$
0.766	0.328	-18.75	0.326	-17.60
1.832	0.370	-21.99	0.370	-22.4

The comparison between the free flight data and CFD solutions shows that the prediction of both static (C_{l_0}) and dynamic (C_{l_p}) derivatives with the least squares method is quite accurate.

When the angle of attack does not equal to zero, from equation (4.3), $C_{l\beta}$ and $C_{lp} + C_{l\dot{\beta}} sin\alpha_0$ derivatives can be calculated by using the least squares method. The sinusoidal oscillating motion is performed with the parameters of $\alpha_0 = 5°$, $\phi_A = 10°$ and $k = \omega d/(2V) = 0.05$ for Mach 1.832. The calculated coefficients are given in the following table.

Table 4.8: Rolling moment coefficients at angle of attack $\alpha_0 = 5°$ with $\phi_A = 10°$ and $k = 0.05$.

Mach Number	C_{l0}	$C_{l\beta} sin\alpha_0$ $[1/rad]$	$C_{lp} + C_{l\dot{\beta}} sin\alpha_0$ $[1/rad]$
1.832	0.387	0.292	-23.179

When the results of oscillating motion with different angles of attacks are examined, the rolling moment coefficient C_{l_0} increases with angle of attack as shown in Table 4.9.

Table 4.9: Rolling moment coefficient C_{l0} at different angle of attacks α_0.

	$\boldsymbol{\alpha_0 = 0°}$	$\boldsymbol{\alpha_0 = 5°}$
$\mathbf{C_{l0}}$	0.370	0.387

4.2.2.2 Prediction of Pitching Moment Coefficients

The variation of pitching moment during sinusoidal oscillating motion about the roll axis is represented in Figure 4.10. As it can be seen from the figure, the pitching moment coefficient changes periodically under the rolling oscillating motion.

It is possible to write the following relationship from equation (2.21).

$$C_m = C_{m0} + \frac{\partial C_m}{\partial \beta} \sin \alpha_0 \theta_x + \left(\frac{\partial C_m}{\partial p} + \frac{\partial C_m}{\partial \dot{\beta}} \sin \alpha_0 \right) \dot{\theta}_x \tag{4.5}$$

After inserting equations (4.1) and (4.2) into equation (4.5), the following equation is obtained.

$$C_m = C_{m0} + C_{m\beta} \sin \alpha_0 \phi_A sin(\omega t) + (C_{mp} + C_{m\dot{\beta}} \sin \alpha_0) \phi_A \omega cos(\omega t) \frac{d}{2V} \tag{4.6}$$

The parameters of $\alpha_0 = 5°$, $\phi_A = 10°$ and $k = \omega d/(2V) = 0.05$ for Mach 1.832 are used to describe the sinusoidal oscillating motion in unsteady computations.

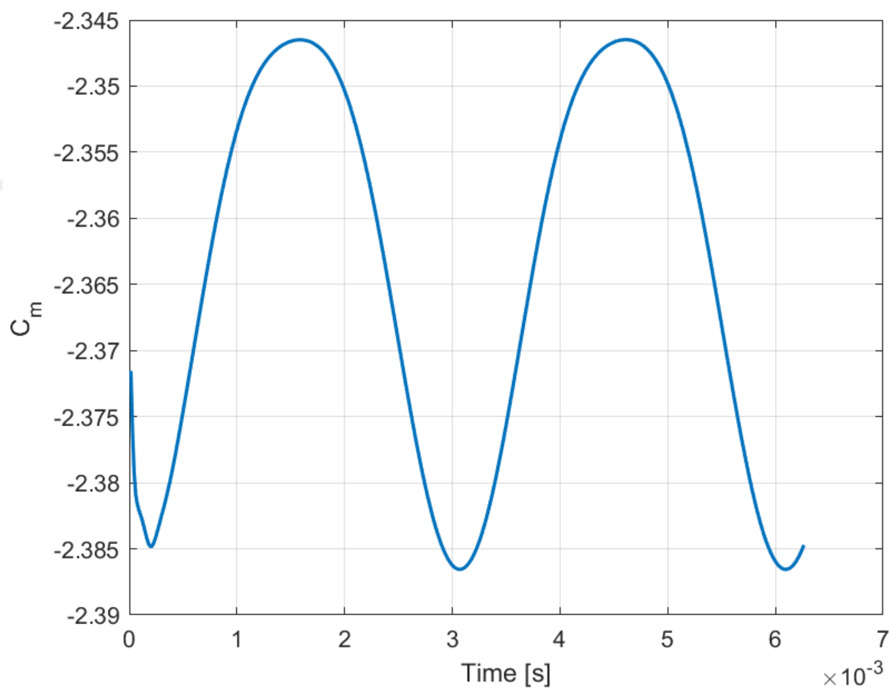

Figure 4.10: Variation of pitch moment coefficient during sinusoidal oscillating motion about roll axis.

The least squares method is applied to solve equation (4.6) by using the second period data of the sinusoidal oscillating motion around the roll axis. The results are presented in Table 4.10.

Table 4.10: Pitch moment coefficients at angle of attack $\alpha_0 = 5°$.

Mach Number	C_{m0}	$C_{m\beta} sin\alpha_0 [1/rad]$	$C_{mp} + C_{m\dot{\beta}} sin\alpha_0 [1/rad]$
1.832	-2.36	-0.12	-2.31

C_{m0} in Table 4.10 refers to the pitching moment coefficient when the angle of attack is equal to $\alpha_0 = 5°$. Therefore, $C_{m\alpha}$ can be calculated as C_{m0}/α_0 which gives $C_{m\alpha} = -0.472\ [1/deg]$. It is observed that this result is very close to the one obtained from steady state computations.

4.3 Unsteady Pitch Analysis

In this part of the thesis, the results of the CFD calculations to predict pitch damping derivatives with different methods are given and discussed. Firstly, the results of the forced oscillation method are introduced.

4.3.1 Forced Oscillation Method

Angle of attack change in the forced oscillation method is given by $\alpha(t) = \alpha_0 + Asin(\omega t)$. The magnitude of the amplitude, A, of pitch movement is usually chosen less than 1° [7]. The unsteady computations are carried out using $A = 0.4°$ and $k = 0.1$ for Mach 0.766 and Mach 1.832. In this study, the mean angle of attack (α_0) is taken as zero for ease of calculations. The nominal number of time steps in order to complete one cycle of forced oscillating motion is chosen as $N = 200$ [7]. The time step for unsteady analysis is determined as;

$$\Delta t = \frac{T}{N} \tag{4.7}$$

where T is the period of the oscillation. It can be calculated from;

$$T = \frac{\pi d}{V k} \tag{4.8}$$

where k is the reduced frequency, d is the diameter of projectile, and V is the freestream velocity.

The forced oscillation motion is firstly applied for three periods for the convergence of unsteady analysis. The angle of attack change during the motion is shown in Figure 4.11.

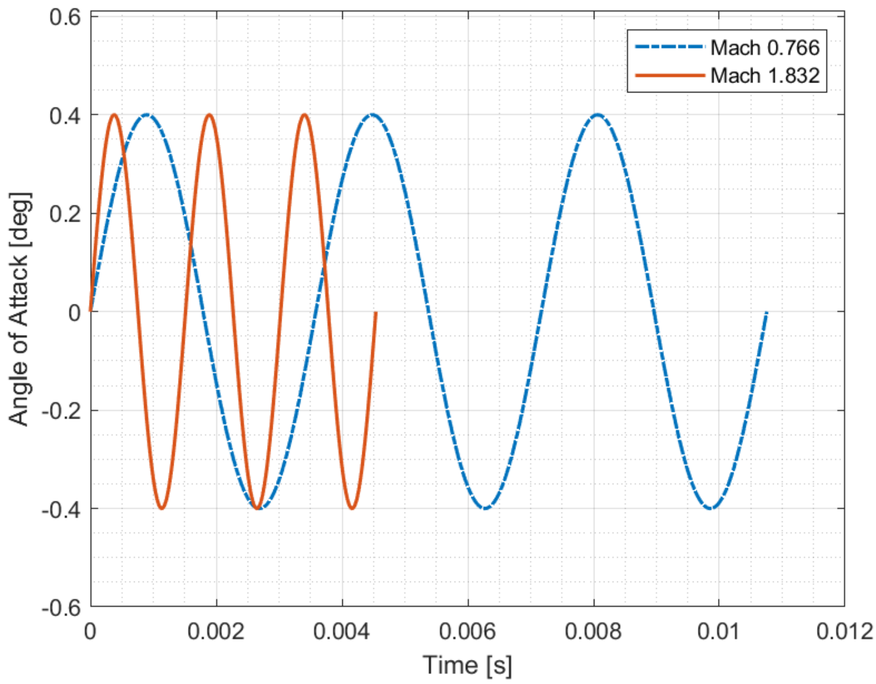

Figure 4.11: Angle of attack change in three periods of forced pitching oscillation.

The pitching moment and normal force coefficients obtained from unsteady computations are represented according to angle of attack in Figures 4.12 and 4.13. The analyzes are carried out using unsteady RANS equations with SA turbulence model and 25 inner iterations.

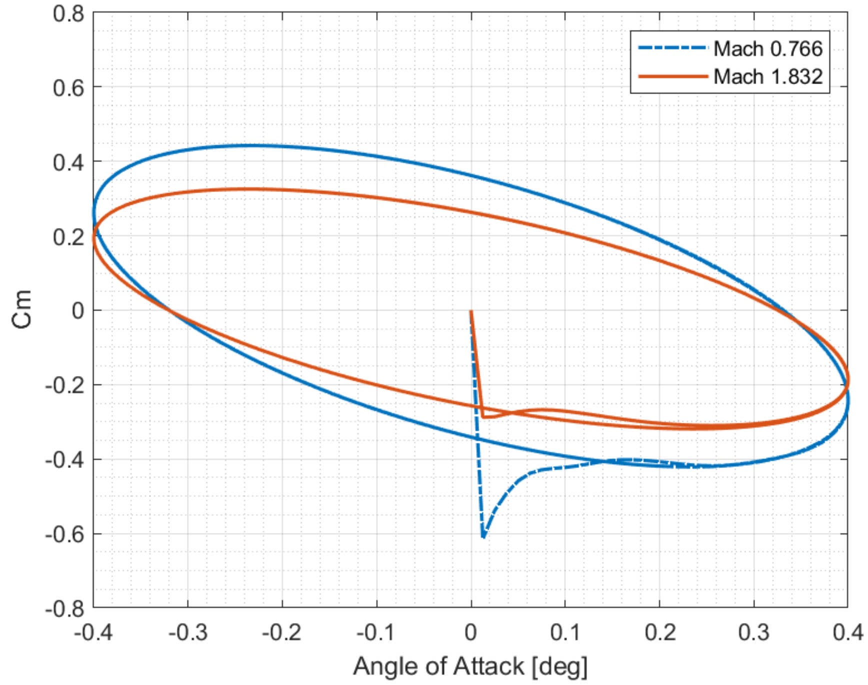

Figure 4.12: Pitching moment coefficient with respect to angle of attack.

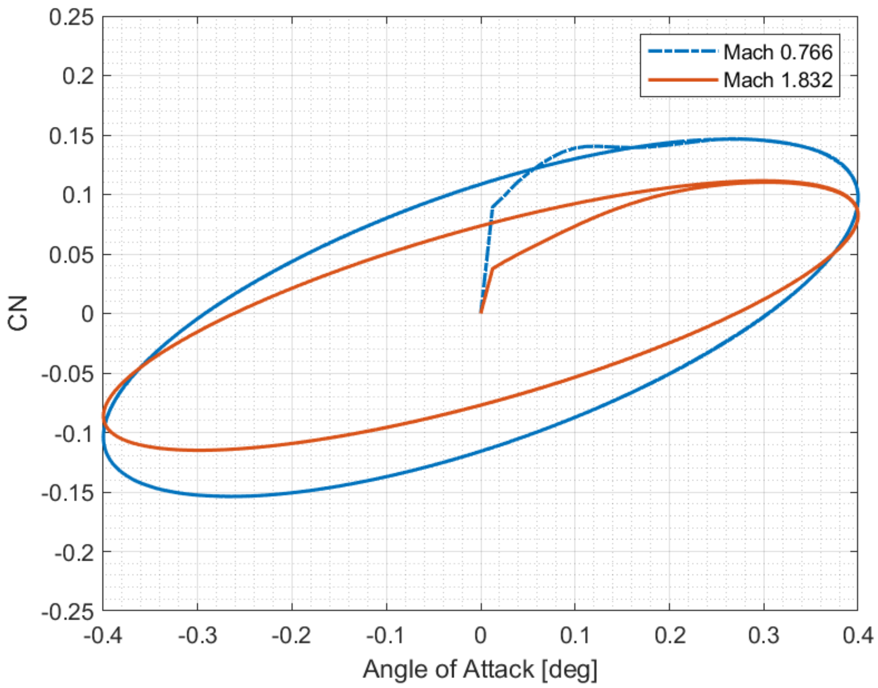

Figure 4.13: Normal force coefficient with respect to angle of attack.

In Figures 4.12 and 4.13, it is observed that after the first period of oscillating motion, the solution becomes quasi-periodic. Thus, two periods of oscillation for this method can be enough. Three different approaches are used to determine pitch damping derivatives from the history of aerodynamic coefficients.

Approach I: Integrating over a Period of Oscillation

By solving equation (2.39), the pitch damping moment coefficient ($C_{mq} + C_{m\dot{\alpha}}$) and the normal force damping coefficient ($C_{Nq} + C_{N\dot{\alpha}}$) are calculated for Mach 0.766 and Mach 1.832. The results are indicated in the following table.

Table 4.11: Results of integrating over a period of oscillation approach.

Mach Number	$C_{mq} + C_{m\dot{\alpha}}[1/rad]$	$C_{Nq} + C_{N\dot{\alpha}}[1/rad]$
0.766	-499.48	160.97
1.832	-372.61	107.93

Approach II: Solving at the Mean Angular Displacement Position

By solving equation (2.43), the pitch damping moment coefficient ($C_{mq} + C_{m\dot{\alpha}}$) and the normal force damping coefficient ($C_{Nq} + C_{N\dot{\alpha}}$) are computed as shown in Table 4.12.

Table 4.12: Results of solving at the mean angular displacement position approach.

Mach Number	$C_{mq} + C_{m\dot{\alpha}}[1/rad]$	$C_{Nq} + C_{N\dot{\alpha}}[1/rad]$
0.766	-498.08	160.09
1.832	-372.58	107.92

Approach III: Least Squares Method

The force and moment coefficients can be formulated as;

$$C_j(t) = C_{j0} + C_{j\alpha}\alpha(t) + C_{jq}\frac{q(t)d}{2V} + C_{j\dot{\alpha}}\frac{\dot{\alpha}(t)d}{2V} \tag{4.9}$$

for $j = N, m$.

By implementing $\alpha(t) = Asin(\omega t)$ and $q = \dot{\alpha}$ relation into equation (4.9), the following relation is obtained.

$$C_j(t) = C_{j0} + C_{j\alpha} Asin(\omega t) + (C_{jq} + C_{j\dot{\alpha}}) \frac{A\omega cos(\omega t)d}{2V} \tag{4.10}$$

Using the second period of pitching motion data, the unknown coefficients C_{j0}, $C_{j\alpha}$ and ($C_{jq} + C_{j\dot{\alpha}}$) can be obtained by applying the linear regression model given in equation (2.32). The results of pitching moment and normal force damping coefficients are presented in Tables 4.13 and 4.14.

Table 4.13: Pitching moment coefficients calculated by least squares method.

Mach Number	C_{m0}	$C_{m\alpha}[1/rad]$	$C_{mq} + C_{m\dot{\alpha}}[1/rad]$	Approximation Error
0.766	-0.0106	-35.91	-498.79	1.3e-03
1.832	-0.0033	-27.23	-372.61	6.3e-05

Table 4.14: Normal force coefficients calculated by least squares method.

Mach Number	C_{N0}	$C_{N\alpha}[1/rad]$	$C_{Nq} + C_{N\dot{\alpha}}[1/rad]$	Approximation Error
0.766	0.0035	14.33	160.71	1.3e-03
1.832	0.0018	12.11	107.92	3.3e-05

The values for C_{m0} and C_{N0} coefficients at zero angle of attack in Tables 4.13 and 4.14 can be considered as numeric error since they are expected to be zero due to axisymmetric geometry of the projectile.

The least squares approach allows that the stability derivatives $C_{m\alpha}$ and $C_{mq} + C_{m\dot{\alpha}}$ can be calculated by using only unsteady computations without the need for steady state solution. However, unsteady RANS analyzes are generally started with steady state analysis solutions for easier convergence. Therefore, it may not be advantageous.

The pitch damping moment and normal damping coefficients calculated with the different approaches used in the forced oscillation method are presented in the Table 4.15 and Table 4.16, respectively.

Table 4.15: Comparison of $C_{mq} + C_{m\dot{\alpha}}$ calculated with different approaches.

$\mathbf{C_{mq} + C_{m\dot{\alpha}}}$ **[1/rad]**	**Mach 0.766**	**Mach 1.832**
Approach I	-499.48	-372.61
Approach II	-498.08	-372.58
Approach III	-498.79	-372.61

Table 4.16: Comparison of $C_{Nq} + C_{N\dot{\alpha}}$ calculated with different approaches.

$\mathbf{C_{Nq} + C_{N\dot{\alpha}}}$ **[1/rad]**	**Mach 0.766**	**Mach 1.832**
Approach I	160.97	107.93
Approach II	160.09	107.92
Approach III	160.71	107.92

It is seen that the coefficients computed with different approaches are very close to each other. In order to find damping derivatives by using the forced oscillation method, the second approach, solving at the mean angular displacement position, is easy to apply after the history of aerodynamic coefficients is obtained from the unsteady computations. Also, the following table is created to examine the difference between CFD calculations based on the second approach with the experimental data.

Table 4.17: Pitch damping moment coefficient comparison between calculated with forced oscillation method and free flight data, $k = 0.1$, $A = 0.4°$.

$\mathbf{C_{mq} + C_{m\dot{\alpha}}}$ **[1/rad]**	**Mach 0.766**	**Mach 1.832**
Forced Oscillation	-498.08	-372.58
Free Flight	-223.60	-377.60

Table 4.17 shows a good agreement between the free flight data and the CFD calculations for Mach 1.832. However, there is a big difference between them for Mach 0.766. A study is conducted to examine the error and to see the effect of the critical parameters used in the CFD calculations on the solution. In this method, these parameters can be considered as turbulence model, reduced frequency and amplitude of the sinusoidal motion.

Even though turbulence models do not effect the stability derivatives as explained before, the effect of turbulence models on the unsteady pitching solution is investigated. Therefore, CFD analyzes are carried out with both turbulence models using $k = 0.1$ and $A = 0.4°$ for Mach 0.766. As a result, the histories of pitching moment coefficient is represented in Figure 4.14.

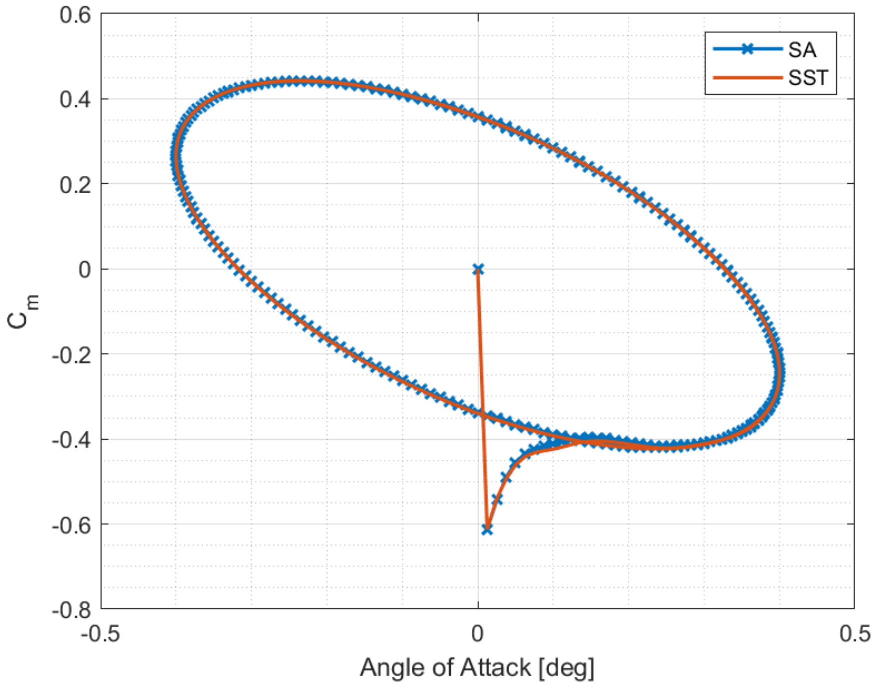

Figure 4.14: C_m vs angle of attack for different turbulence models for 0.766 Mach.

Figure 4.14 indicates that there is no difference between the solutions of both turbulence models.

In order to investigate the reduced frequency effect on the solutions, the forced oscillation analyzes are performed with different reduced frequencies. The amplitude of the oscillating motion remains constant as $A = 0.4°$. The solutions of the pitching moment and normal force coefficients with varying reduced frequencies are presented in Figures 4.15 and 4.16 for Mach 1.832 and in Figures 4.17 and 4.18 for Mach 0.766, respectively.

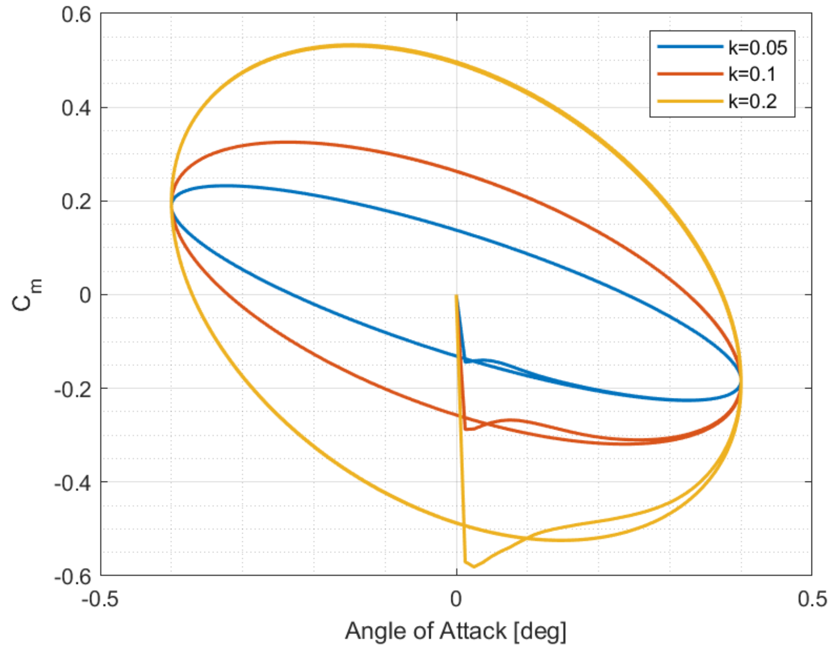

Figure 4.15: Effect of reduced frequency on pitching moment coefficient for Mach 1.832, $A = 0.4°$.

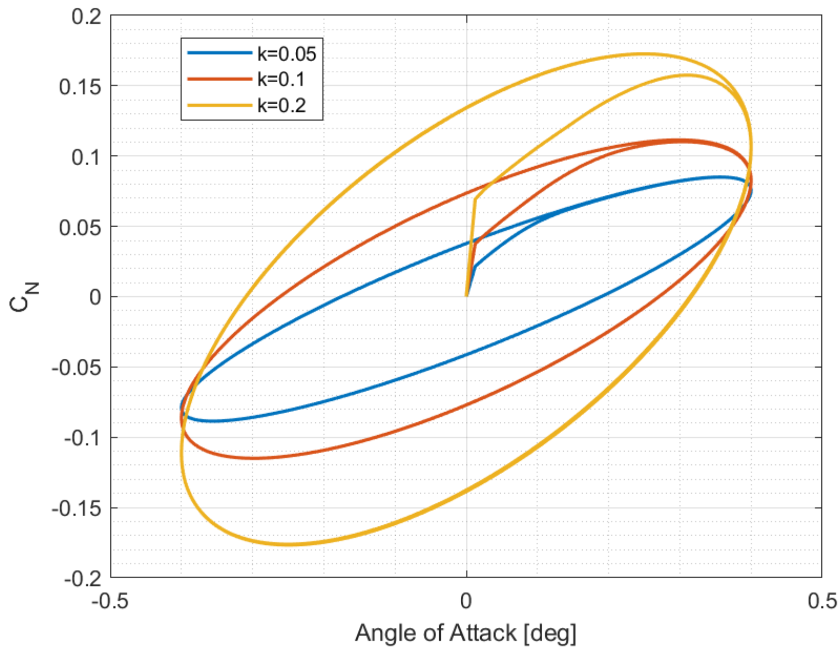

Figure 4.16: Effect of reduced frequency on normal force coefficient for Mach 1.832, $A = 0.4°$.

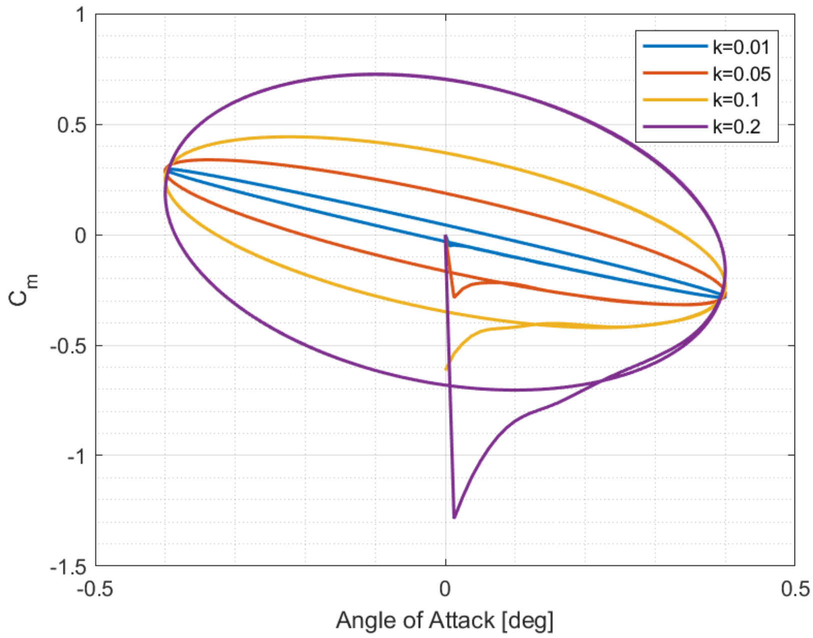

Figure 4.17: Effect of reduced frequency on pitching moment coefficient for Mach 0.766, $A = 0.4°$.

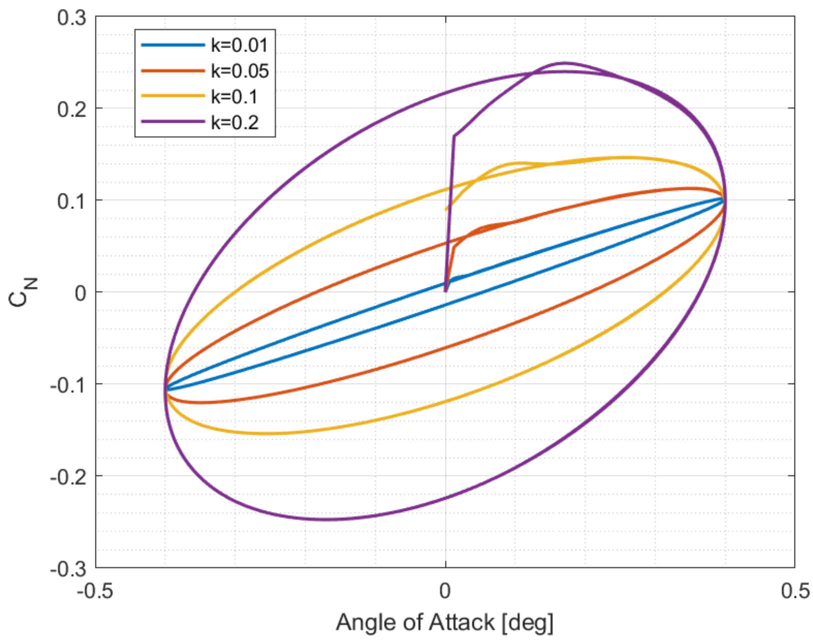

Figure 4.18: Effect of reduced frequency on normal force coefficient for Mach 0.766, $A = 0.4°$.

Since $k = 0.01$ gives a better approximation for the computation of roll damping coefficient at Mach 0.766, the effect of this reduced frequency on the pitch damping coefficient calculation is also investigated. As it can be seen from the above figures, increasing the reduced frequency causes the ellipse loops to narrow. Lowering the reduced frequency excessively can lead to numerical errors to predominate in CFD calculations because the aerodynamic coefficients become too small. On the other hand, when the reduced frequency is increased too much, it can increase the nonlinearity in the flow domain.

The pitch damping derivatives ($C_{mq} + C_{m\dot{\alpha}}$) and normal force damping derivatives ($C_{Nq} + C_{N\dot{\alpha}}$) are calculated for each reduced frequencies for both Mach numbers. They are presented in Tables 4.18 and 4.19.

Table 4.18: CFD calculations of pitch damping coefficients for different reduced frequencies for Mach 0.766, $A = 0.4°$.

Damping Coefficients	$k = 0.01$	$k = 0.05$	$k = 0.1$	$k = 0.2$
$C_{mq} + C_{m\dot{\alpha}}$ $[1/rad]$	-537.93	-505.40	-498.08	-495.00
$C_{Nq} + C_{N\dot{\alpha}}$ $[1/rad]$	168.89	162.97	160.09	157.79

Table 4.19: CFD calculations of pitch damping coefficients for different reduced frequencies for Mach 1.832, $A = 0.4°$.

Damping Coefficients	$k = 0.05$	$k = 0.1$	$k = 0.2$
$C_{mq} + C_{m\dot{\alpha}}$ $[1/rad]$	-385.00	-372.58	-350.99
$C_{Nq} + C_{N\dot{\alpha}}$ $[1/rad]$	113.35	107.92	97.33

The variation of pitch damping moment coefficient and normal force damping coefficient with respect to reduced frequency is presented in Figure 4.19 and Figure 4.20 respectively.

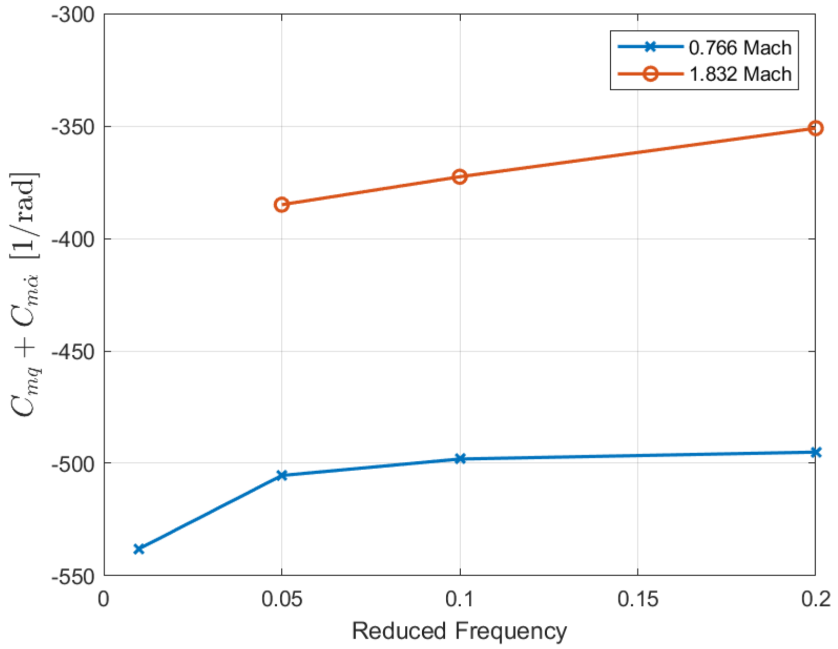

Figure 4.19: Pitch damping moment coefficient $C_{mq} + C_{m\dot{\alpha}}$ $[1/rad]$ according to reduced frequency change.

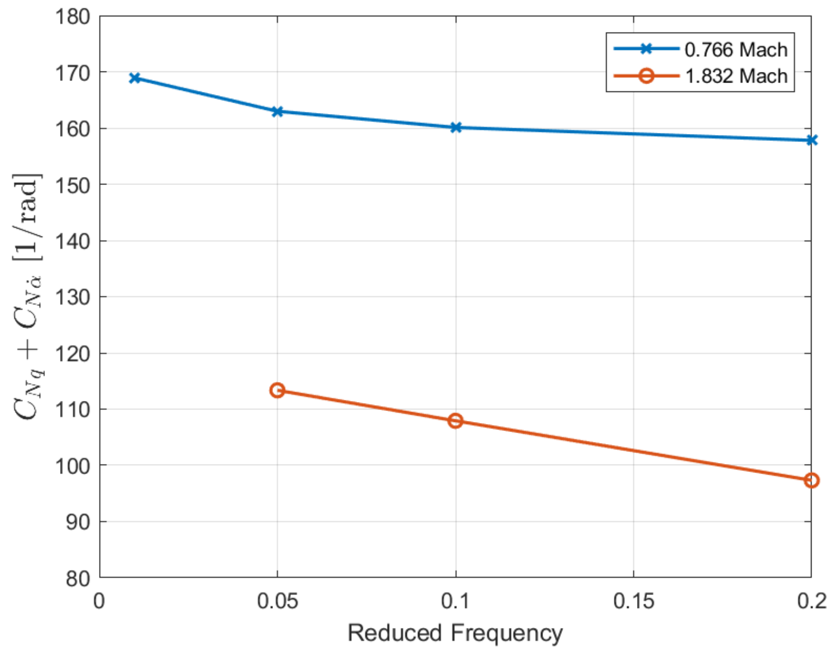

Figure 4.20: Normal force damping coefficient $C_{Nq} + C_{N\dot{\alpha}}$ $[1/rad]$ according to reduced frequency change.

As it can be seen from the above figures, the pitch damping moment coefficient increases as the reduced frequency increases. On the other hand, the normal force damping derivatives decreases as the reduced frequency raises. Also, the pitch moment and normal force dynamic derivatives change almost linearly with respect to examined reduced frequency range for Mach 1.832 . However, the nonlinearity occurs in the case of Mach 0.766, especially when reduced frequency is equal to 0.01.

The effect of the oscillation amplitude parameter of the forced oscillation method is also examined. The unsteady CFD calculations are performed using different amplitudes with constant reduced frequency of $k = 0.1$. For Mach 1.832, the amplitudes of $A = 0.4°$ and $A = 1.0°$ are used. In addition to these amplitudes, $A = 0.2°$ is also tested for Mach 0.766. The variation of pitch moment and normal force coefficients with respect to angle of attack for different oscillation amplitudes for Mach 0.766 are presented in Figures 4.21 and 4.22 respectively. In Figures 4.23 and 4.24, the coefficients for Mach 1.832 are indicated. As the amplitude increases, the angle of attack during the oscillating motion increases which leads to higher aerodynamic force and moment coefficients.

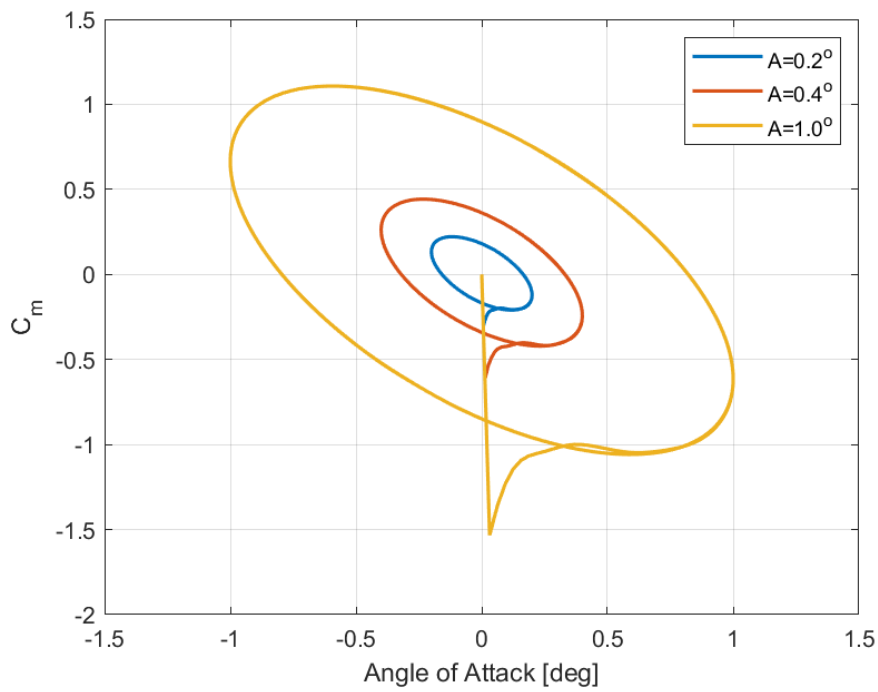

Figure 4.21: Effect of amplitude on pitching moment coefficient for Mach 0.766.

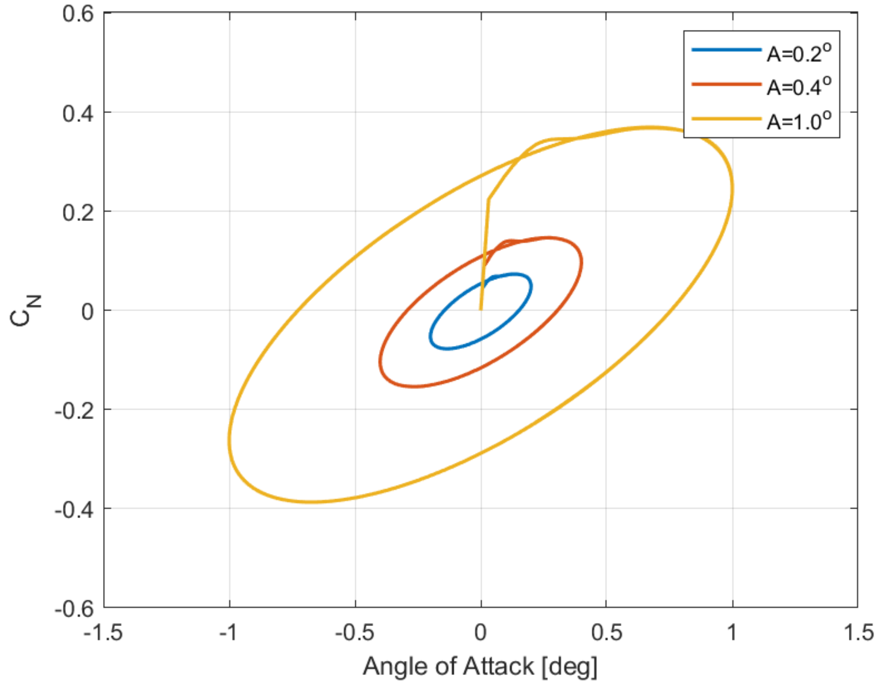

Figure 4.22: Effect of amplitude on normal force coefficient for Mach 0.766.

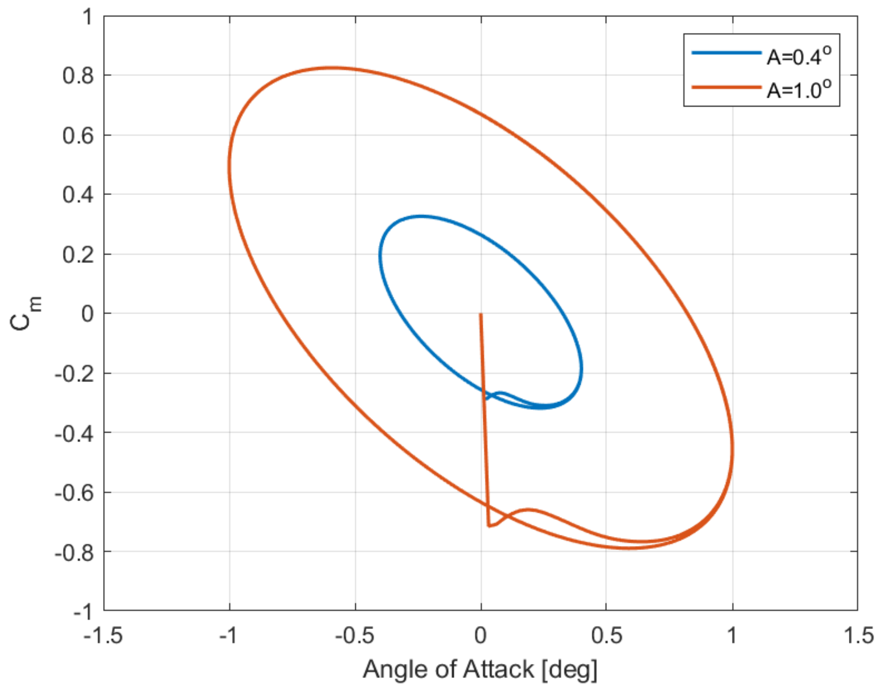

Figure 4.23: Effect of amplitude on pitching moment coefficient for Mach 1.832.

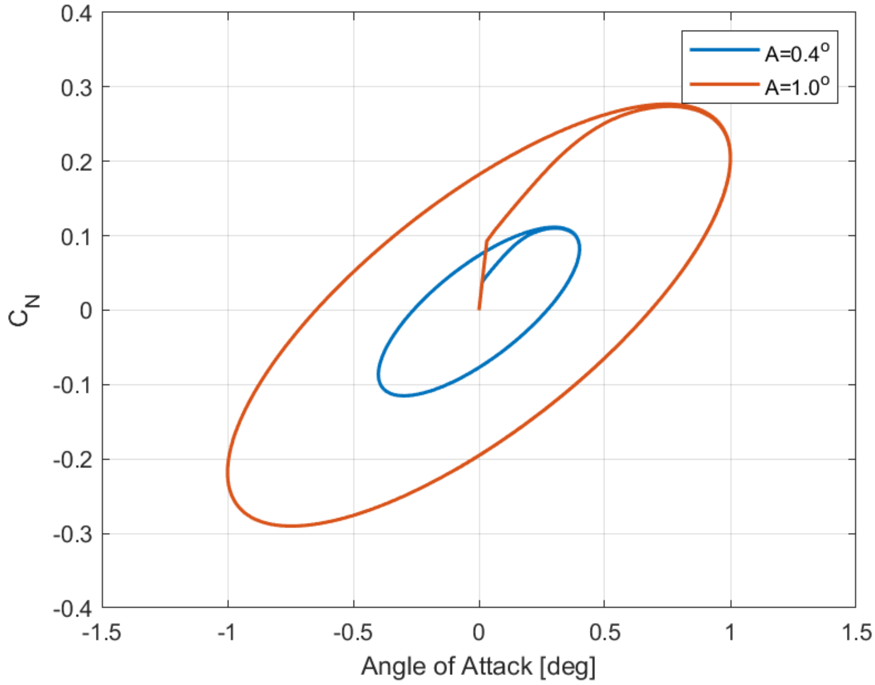

Figure 4.24: Effect of amplitude on normal force coefficient for Mach 1.832.

The coefficients of pitch damping moment derivatives and normal force damping derivatives are computed for different oscillation amplitudes for both Mach numbers. They are presented in Tables 4.20 and 4.21.

Table 4.20: Pitch damping coefficients for different amplitudes for Mach 0.766, $k = 0.1$.

Damping Coefficients	$A = 0.2°$	$A = 0.4°$	$A = 1.0°$
$C_{mq} + C_{m\dot{\alpha}}$	-499.81	-498.08	-500.37
$C_{Nq} + C_{N\dot{\alpha}}$	160.81	160.09	160.29

Table 4.21: Pitch damping coefficients for different amplitudes for Mach 1.832, $k = 0.1$.

Damping Coefficients	$A = 0.4°$	$A = 1.0°$
$C_{mq} + C_{m\dot{\alpha}}$	-372.58	-373.55
$C_{Nq} + C_{N\dot{\alpha}}$	107.92	108.17

Tables 4.20 and 4.21 show that the pitch damping coefficients do not change significantly with different oscillation amplitudes.

Since there is a significant difference between the experimental data and CFD computations of pitch damping moment coefficients for Mach 0.766, the time step of the unsteady RANS calculations is reduced by changing N, the nominal number of time steps in order to complete one cycle. As a result, the time step is halved by increasing the N number from 200 to 400. The reduced frequency and oscillation amplitude for this study is used as $k = 0.1$ and $A = 0.4°$.

Table 4.22: Pitch damping coefficients for different time steps for Mach 0.766, $k = 0.1$, $A = 0.4°$.

Damping Coefficients	$\Delta t = 1.792e - 05\ s$	$\Delta t = 9.047e - 06\ s$
$C_{mq} + C_{m\dot{\alpha}}$	-498.08	-489.17
$C_{Nq} + C_{N\dot{\alpha}}$	160.09	156.92

Table 4.22 shows that the decreasing simulation time step causes a slight change in the pitch damping coefficients.

4.3.2 Differential Method

Another method to predict pitch damping derivatives is the differential method. In order to apply differential method using equation (2.47), two unsteady analyzes under constant pitching angular velocities are performed. The pitching angular velocities are determined to reach the same angle of attack after a certain time as indicated in equation (4.11). As an example, pitch rates are chosen as $q_1 = 0.2\ rad/s$ and $q_2 = 0.4\ rad/s$. The expected angle of attack after the pitching motion is $\Delta\alpha = 0.004\ rad$. Therefore, the simulation time required to complete this motion is determined from equation (4.11).

$$\Delta\alpha = q_1 t_1 = q_2 t_2 \tag{4.11}$$

The unsteady calculations are performed for Mach numbers of 0.766 and 1.832. The change of the normal force coefficients under constant pitching angular velocities for both Mach numbers is shown in Figure 4.25. Similarly, the change of pitching moment coefficients is presented in Figure 4.26. From the figures, it is observed that the pitching moment and normal force coefficients changes linearly after some transition iterations.

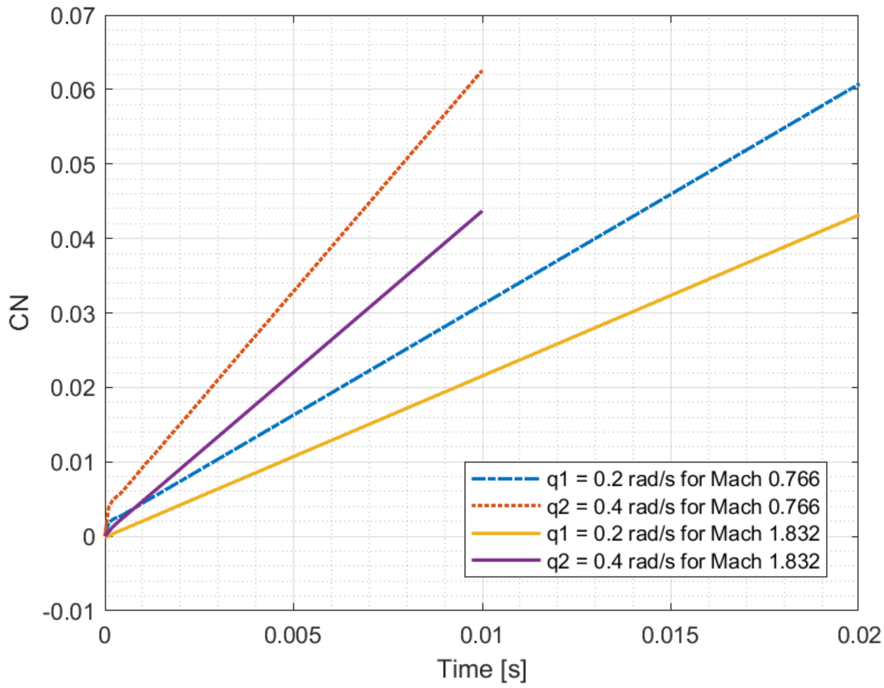

Figure 4.25: Normal force coefficient change under constant pitching angular rates.

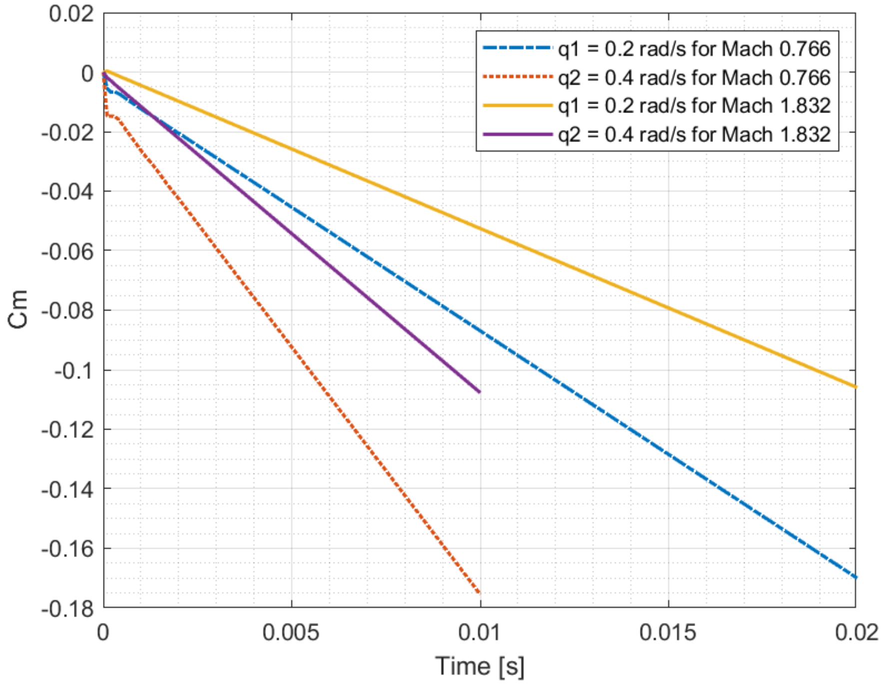

Figure 4.26: Pitch moment coefficient change under constant pitching angular rates.

The pitch damping derivatives are calculated by using equation (2.47). The results are given in Table 4.23.

Table 4.23: Prediction of pitch damping derivatives with the differential method.

Mach Number	$C_{mq} + C_{m\dot{\alpha}}$ $[1/rad]$	$C_{Nq} + C_{N\dot{\alpha}}$ $[1/rad]$
0.766	-478.00	156.54
1.832	-360.10	106.19

Since the normal force coefficient and pitching moment coefficient change linearly with time after some transient iterations, the expected angle of attack value for this case, and hence the simulation time, can be halved. That means the simulation time can be reduced using the same angular velocities and the new angle of attack $\Delta\alpha = 0.002\ rad$. For this case, the pitch damping derivative for Mach 1.832 is computed as $(C_{mq} + C_{m\dot{\alpha}}) = -360.07\ [1/rad]$. As a result, the iteration numbers required for this method can be chosen less that results in lower computational cost.

Since the pitch damping moment derivatives of the free flight experimental data [2] are available, the pitch damping moment derivatives calculated by different prediction methods are compared with the free flight experimental data in Table 4.24.

Table 4.24: Comparison of the pitch damping derivatives ($C_{mq} + C_{m\dot{\alpha}}$ $[1/rad]$) between CFD calculations and experimental data.

	Mach 0.766	**Mach 1.832**
Forced Oscillation Method	-503.58	-372.58
Differential Method	-478.00	-360.10
Free Flight Data	-223.60	-377.60

It is noted that the results of the forced oscillation method is given in Table 4.24 for $k = 0.1$ and $A = 0.4°$.

The relative errors of the numerical prediction methods with respect to free flight test data are presented in the following table.

Table 4.25: Relative error [%] of the numerical methods with respect to free flight data.

	Mach 0.766	**Mach 1.832**
Forced Oscillation Method	125.2	1.3
Differential Method	113.8	4.6

Table 4.25 shows that the prediction of damping derivative with these two methods is quite accurate for Mach 1.832. However, there is a big difference between CFD calculations and free flight data for Mach 0.766. The predicted pitch damping moment coefficients by SU2 computations for different Mach numbers are represented in Figure 4.27. Also, the single fit (FF-SF) and multiple fit (FF-MF) free flight data are included in the figure. In addition to these, the results of the calculations of pitch damping coefficients by using CFD++ software in reference [7] are indicated in the same figure.

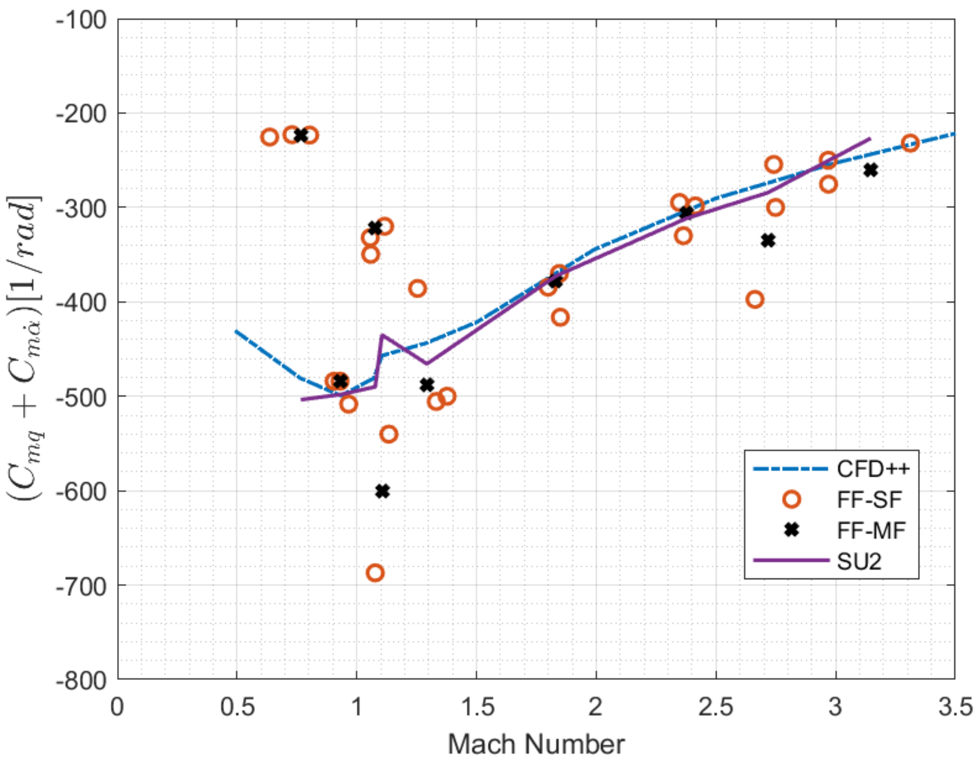

Figure 4.27: Comparison of pitch damping moment derivatives according to Mach Number.

The general trend of the results obtained using SU2 and CFD++ are very similar. There is a significant difference between CFD results and experimental data in subsonic and transonic region. Reference [2] states that due to the low angle of attack, large variation in C_{m_q} and C_{N_α} coefficients occurs. The pitch damping moment coefficient are obtained from multiple fit approach with the standard deviation errors of the order of 10% [2]. There is high scatter in the free flight data for this coefficient. Also, in reference [7], it is stated that the accuracy of free flight test data at subsonic speeds and low transonic speeds can be uncertain due to large standard deviation errors.

4.3.3 Plunging Oscillation Method

The single translational pitch dynamic derivatives $C_{m\dot{\alpha}}$ and $C_{N\dot{\alpha}}$ can be computed by applying a small plunging oscillation. The motion of the plunging oscillation is defined as; $\boldsymbol{z}(t) = \boldsymbol{z}_m \sin(\omega t)$ where z_m is the plunging oscillation amplitude and ω is the plunging angular velocity. The unsteady computations are performed with the reduced frequency of $k = 0.05$ and the plunging amplitude of $z_m = 0.015\ m$ which is equal to the radius of the basic finner projectile. The plunging oscillating motion is applied for three periods. The variation of the pitching moment coefficient with respect to angle of attack and angle of attack rate for both Mach numbers is presented in Figures 4.28 and 4.29. The figures show that after the first period of oscillating motion, the solution becomes quasi-periodic as in the case of pitching oscillatory motion. Therefore, two periods of oscillation can be enough.

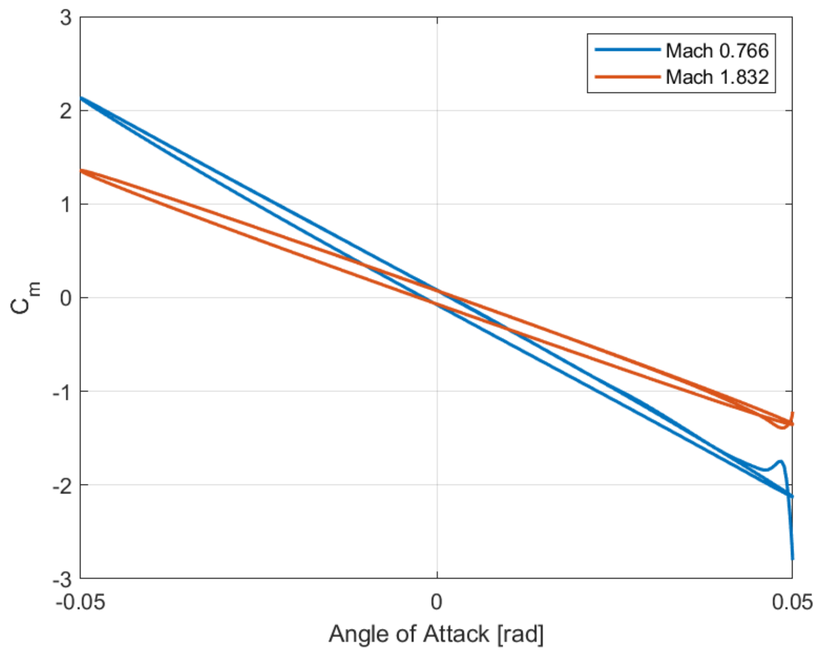

Figure 4.28: Pitching moment coefficient change with respect to angle of attack during plunge motion, $k = 0.05$ and $z_m = 0.015\ m$.

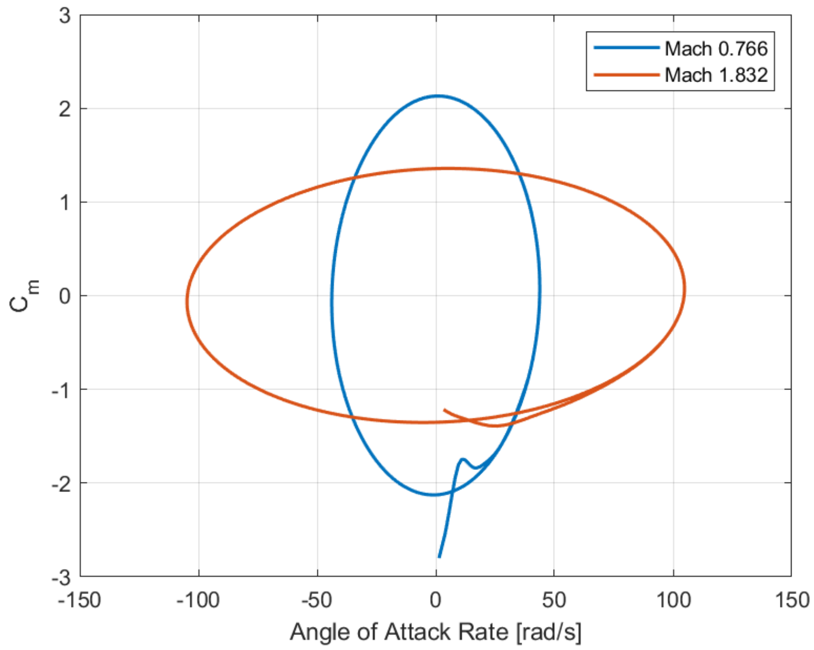

Figure 4.29: Pitching moment coefficient change with respect to angle of attack rate during plunge motion, $k = 0.05$ and $z_m = 0.015\ m$..

By using equation (2.54), the dynamic derivatives of $C_{m\dot{\alpha}}$ and $C_{N\dot{\alpha}}$ can be calculated. Also, it is possible to use the least squares method to predict aerodynamic stability derivatives. The calculated single dynamic derivatives by using equation (2.54) are presented in the following table. The computations are made for $k = 0.05$ and $z_m = 0.015\ m$.

Table 4.26: Calculated $C_{m\dot{\alpha}}$ and $C_{N\dot{\alpha}}$ coefficients, $k = 0.05$ and $z_m = 0.015\ m$.

Mach Number	$C_{N\dot{\alpha}}$ $[1/rad]$	$C_{m\dot{\alpha}}$ $[1/rad]$
0.766	38.60	-31.75
1.832	34.28	-30.28

Also, the least squares method can be used to determine C_{j0}, $C_{j\alpha}$ and $C_{j\dot{\alpha}}$ coefficients in equation (2.53) where $j = N, m$. The results obtained by this method are shown in the following table. C_{j0} can be assumed to be negligible due to axisymmetric geometry of the basic finner configuration.

Table 4.27: Calculated aerodynamic coefficients with least squares method, $k = 0.05$ and $z_m = 0.015\ m$.

Mach Number	$C_{N\alpha}$ $[1/rad]$	$C_{N\dot{\alpha}}$ $[1/rad]$	$C_{m\alpha}$ $[1/rad]$	$C_{m\dot{\alpha}}$ $[1/rad]$
0.766	15.56	37.56	-42.23	-27.86
1.832	11.64	33.80	-27.04	-28.53

When Table 4.26 and Table 4.27 are compared, it is observed that the derivatives of $C_{m\dot{\alpha}}$ and $C_{N\dot{\alpha}}$ calculated using equation (2.54) and the derivatives computed with the least squares method are very close to each other. Also, the static stability derivatives $C_{N\alpha}$ and $C_{m\alpha}$ calculated using the least squares method presented in Table 4.27 can be compared with free flight experimental data shown in Table 4.28. The comparison between them shows that the static stability derivatives calculated with the least squares method during the plunging oscillating motion are similar to the free flight data.

Table 4.28: $C_{N\alpha}$ and $C_{m\alpha}$ coefficients of free flight data.

Mach Number	$C_{N\alpha}$ $[1/rad]$	$C_{m\alpha}$ $[1/rad]$
0.766	16.70	-40.8
1.832	11.8	-28.0

Also, the effect of the reduced frequency and plunging amplitude on unsteady calculations is investigated. The unsteady CFD analyzes are performed with the reduced frequencies of $k = 0.025$, $k = 0.05$ and $k = 0.1$. The pitching moment coefficient change with respect to angle of attack for different reduced frequencies for Mach 0.766 and Mach 1.832 is shown in Figures 4.30 and 4.31.

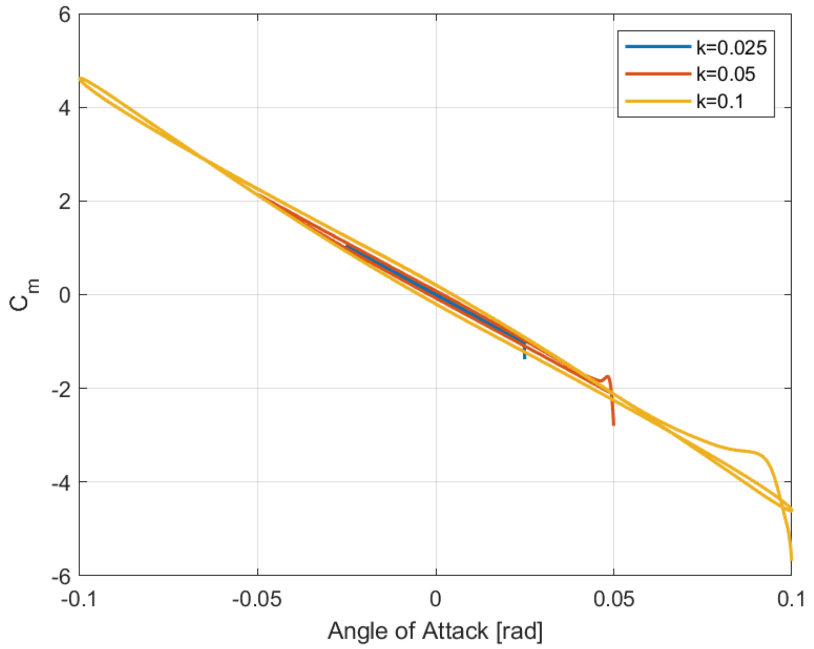

Figure 4.30: Pitching moment coefficient with respect to angle of attack for different reduced frequencies for Mach 0.766, $z_m = 0.015\ m$.

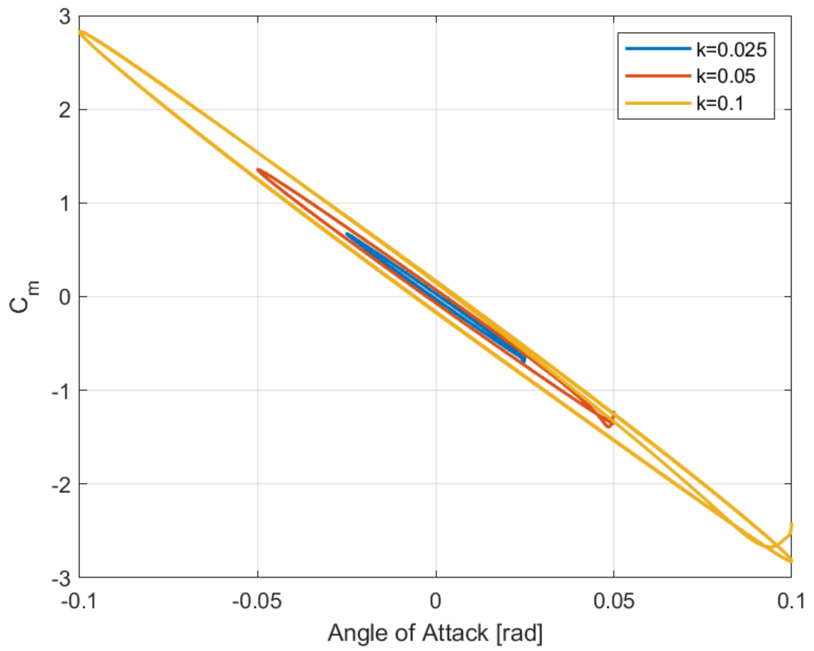

Figure 4.31: Pitching moment coefficient with respect to angle of attack for different reduced frequencies for Mach 1.832, $z_m = 0.015\ m$.

From Figures 4.30 and 4.31, it is apparent that the variation of C_m coefficient with respect to angle of attack for the plunge motion is more slimmer than for the pitching motion. Therefore, the variation of the C_m coefficient with respect to the angle of attack rate for different reduced frequencies for Mach 1.832 is also shown in Figure 4.32. Since the variation for Mach 0.766 is similar to Figure 4.32, it is not shown.

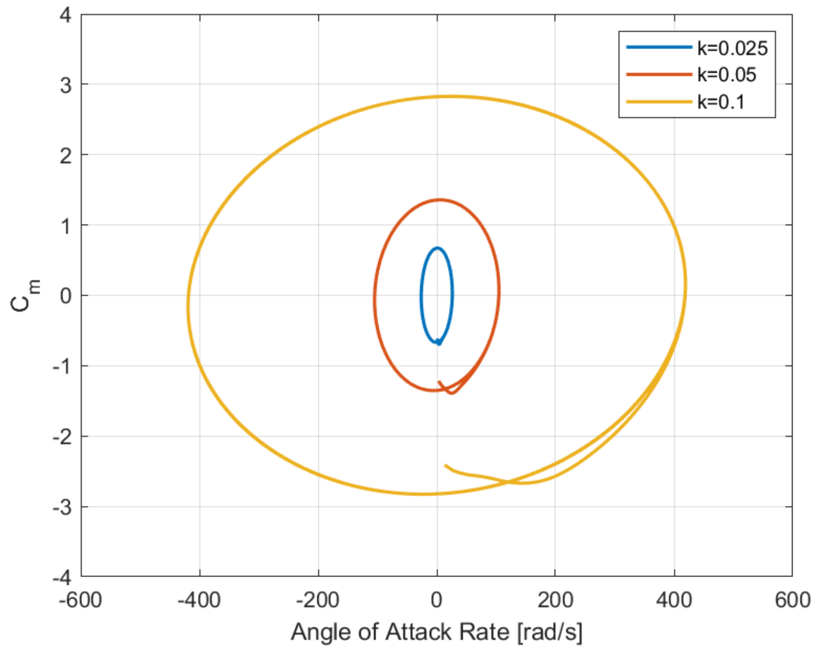

Figure 4.32: Pitch moment coefficient with respect to angle of attack rate for different reduced frequencies for Mach 1.832, $z_m = 0.015\ m$.

The calculated $C_{m\dot{\alpha}}$ and $C_{N\dot{\alpha}}$ for different reduced frequencies are presented in Tables 4.29 and 4.30 for both Mach numbers.

Table 4.29: $C_{m\dot{\alpha}}$ and $C_{N\dot{\alpha}}$ coefficients for different reduced frequencies for Mach 0.766, $z_m = 0.015\ m$.

Damping Coefficients	$k = 0.025$	$k = 0.05$	$k = 0.1$
$C_{m\dot{\alpha}}$ $[1/rad]$	-55.61	-31.75	-19.71
$C_{N\dot{\alpha}}$ $[1/rad]$	47.71	38.60	33.54

Table 4.30: $C_{m\dot{\alpha}}$ and $C_{N\dot{\alpha}}$ coefficients for different reduced frequencies for Mach 1.832, $z_m = 0.015\ m$.

Damping Coefficients	$k = 0.025$	$k = 0.5$	$k = 0.1$
$C_{m\dot{\alpha}}$ $[1/rad]$	-47.88	-30.28	-16.91
$C_{N\dot{\alpha}}$ $[1/rad]$	41.65	34.28	28.84

Figure 4.33 indicates the variation of the derivative of the pitch damping moment with respect to reduced frequency. As in the case of forced oscillation method, when the reduced frequency increases, the derivative of $C_{m\dot{\alpha}}$ increases. On the contrary, increasing reduced frequency leads to decrease in the derivative of $C_{N\dot{\alpha}}$.

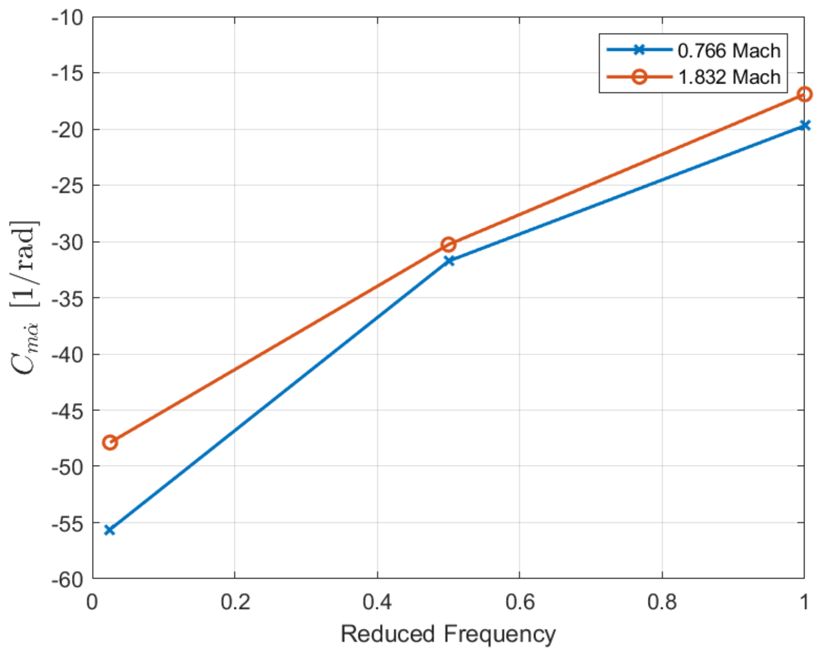

Figure 4.33: Pitch damping moment coefficient change with respect to different reduced frequencies.

Also, the effect of the plunging amplitude parameter on the unsteady computations is examined. Two different plunging amplitudes of $z_m = 0.015\ m$ and $z_m = 0.030\ m$ are used for this study. To illustrate the effect of the plunging oscillation amplitude on the pitching moment coefficient for Mach 1.832, the results of the unsteady calculations are presented in Figure 4.34. The similar behavior is observed for Mach 0.766

as well.

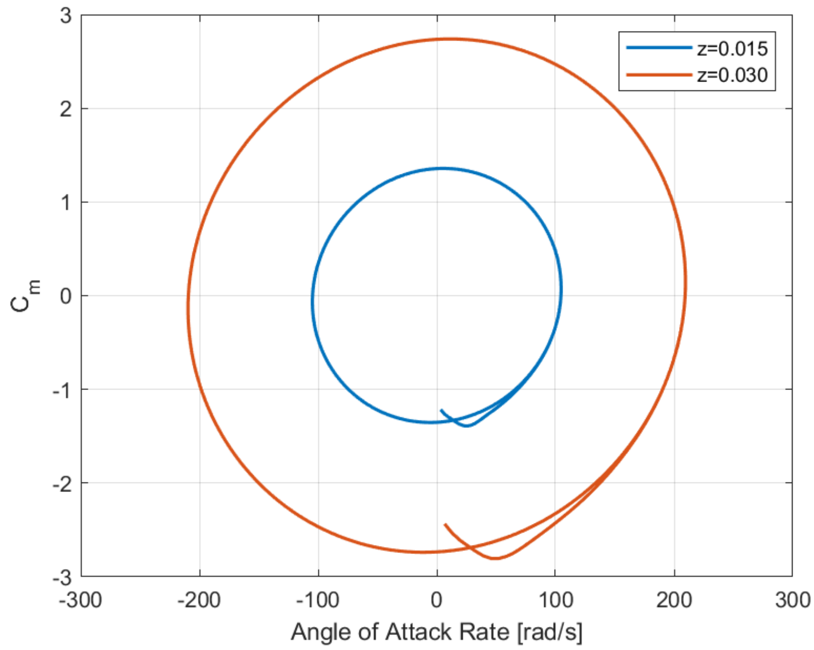

Figure 4.34: Pitch moment coefficient change with respect to different plunging oscillation amplitudes for Mach 1.832, $k = 0.05$.

The dynamic derivatives of $C_{m\dot{\alpha}}$ and $C_{N\dot{\alpha}}$ coefficients for different oscillation amplitudes are calculated for both Mach numbers and represented in Tables 4.31 and 4.32. The results in the tables indicates that the dynamic derivatives of $C_{m\dot{\alpha}}$ and $C_{N\dot{\alpha}}$ do not change significantly with plunging oscillation amplitudes.

Table 4.31: $C_{m\dot{\alpha}}$ and $C_{N\dot{\alpha}}$ coefficients for different plunging oscillation amplitudes for Mach 0.766, $k = 0.05$.

Damping Coefficients	$z = 0.015\ m$	$z = 0.030\ m$
$C_{m\dot{\alpha}}$ $[1/rad]$	-31.75	-30.62
$C_{N\dot{\alpha}}$ $[1/rad]$	38.60	38.26

Table 4.32: $C_{m\dot{\alpha}}$ and $C_{N\dot{\alpha}}$ coefficients for different plunging oscillation amplitudes for Mach 1.832.

Damping Coefficients	$z = 0.015\ m$	$z = 0.030\ m$
$C_{m\dot{\alpha}}$ $[1/rad]$	-30.28	-29.50
$C_{N\dot{\alpha}}$ $[1/rad]$	34.28	34.05

Also it is noted that the single dynamic stability derivatives of C_{mq} and C_{Nq} can be calculated by subtracting $C_{m\dot{\alpha}}$ and $C_{N\dot{\alpha}}$ derivatives from the combined derivatives of $C_{mq} + C_{m\dot{\alpha}}$ and $C_{Nq} + C_{N\dot{\alpha}}$.

CHAPTER 5

CONCLUSION

In this thesis, the numerical prediction methods used to calculate aerodynamic stability derivatives, using the SU2 software are explained. By using the basic finner projectile from literature, the validation studies are carried out. The calculation method of static stability derivatives is mentioned. The effect of the turbulence models of SA and SST on the steady and unsteady calculations is examined. As a result of the analyzes using two different turbulence models, it is seen that the choice of turbulence model does not have a significant effect on the aerodynamic coefficients except for axial force coefficient. Although there are some differences between the solutions of both turbulence models in the flow field, there is no difference observed between the aerodynamic stability derivatives since they are integral values of CFD computations. Most of the analyzes in this thesis are carried out using SA turbulence model because the computational cost of the SA model is lower.

Also, the numerical prediction methods to calculate roll damping coefficients are emphasized. It is observed that the results obtained by using the rigid mesh motion and rotating reference frame options are very close to each other. However, the rotating reference frame can be preferred because it provides a steady state solution. The effect of the reduced frequency is also investigated. It is observed that the reduced frequency for unsteady computations under constant roll rate does not significantly affect the solution in the supersonic regime whereas it may be important for the subsonic regime since decreasing reduced frequency leads to better approximation for roll damping coefficient.

In addition, the prediction methods that are based on forced oscillatory motion and differential method are emphasized in order to calculate pitch damping coefficients.

Different approaches, that are integrating over a period of oscillation, solving at the mean angular displacement position and the least squares method, are used to calculate the combined pitch damping derivatives from the history of the aerodynamic coefficients obtained from the forced oscillation method. The effect of the parameters of the oscillating method such as reduced frequency and amplitude is also examined. It is observed that the variation of the reduced frequency affects the solutions of the forced oscillating motion. The increase in reduced frequency leads to a decrease in the normal force damping coefficients but an increase in the pitch damping moment coefficients. When the effect of amplitude on pitch damping derivative calculation is investigated, it is seen that this parameter does not have a significant effect on the solutions. In addition to the forced oscillation method, the differential method can be used to calculate pitching dynamic derivatives. This method can provide a faster prediction of pitch damping derivatives for small angle of attacks with some compromise in accuracy. Moreover, the plunging oscillation method is emphasized to calculate single translational pitch dynamic derivatives. The effect of the plunging oscillation amplitude and the reduced frequency on the solutions is investigated. It is observed that translational pitch damping derivatives do not change significantly with plunging oscillation amplitudes whereas the reduced frequency variation affects the solution similar to the combined pitch damping moment calculation.

It is also noted that the least squares method is a very powerful method that enables the calculation of aerodynamic stability derivatives from the history of aerodynamic coefficients corresponding to varying flight conditions during the oscillating motions. To conclude, the results of the CFD analyzes are compared with the experimental data, and it is observed that there is good agreement between experimental data and CFD calculations.

REFERENCES

[1] F. Wang and L. Chen, "Numerical prediction of stability derivatives for complex configurations," *Procedia Engineering*, vol. 99, pp. 1561–1575, 2015.

[2] A. Dupuis, "Aeroballistic range and wind tunnel tests of the basic finner reference projectile from subsonic to high supersonic velocities," *Defense Research and Development Canada TR, Saint-Gabriel-de-Valcartier, QC, Canada*, 2002.

[3] X. Huang, "Wing and fin buffet on the standard dynamics model," tech. rep., FIELD TECHNOLOGY INC LONG BEACH CA, 2000.

[4] D. D. Vicroy, T. D. Loeser, and A. Schütte, "Static and forced-oscillation tests of a generic unmanned combat air vehicle," *Journal of Aircraft*, vol. 49, no. 6, pp. 1558–1583, 2012.

[5] B.-g. Mi, H. Zhan, and B.-b. Chen, "New systematic cfd methods to calculate static and single dynamic stability derivatives of aircraft," *Mathematical Problems in Engineering*, vol. 2017, 2017.

[6] B. Mi and H. Zhan, "Review of numerical simulations on aircraft dynamic stability derivatives," *Archives of Computational Methods in Engineering*, vol. 27, no. 5, pp. 1515–1544, 2020.

[7] V. A. Bhagwandin and J. Sahu, "Numerical prediction of pitch damping stability derivatives for finned projectiles," *Journal of Spacecraft and Rockets*, vol. 51, no. 5, pp. 1603–1618, 2014.

[8] B. Mi, H. Zhan, and B. Chen, "Calculating dynamic derivatives of flight vehicle with new engineering strategies," *International Journal of Aeronautical and Space Sciences*, vol. 18, no. 2, pp. 175–185, 2017.

[9] B. L. Uselton and L. M. Jenke, "Experimental missile pitch-and moll-damping characteristics at large," *Journal of Spacecraft and Rockets*, vol. 14, no. 4, pp. 241–247, 1977.

[10] M. Beyers, "Subsonic roll oscillation experiments on the standard dynamics model," in *10th Atmospheric Flight Mechanics Conference*, p. 2134, 1983.

[11] C. Jermey and L. SCHIFF, "Wind-tunnel investigation of the aerodynamic characteristics of the standard dynamics model in coning motion at mach 0.6," in *12th Atmospheric Flight Mechanics Conference*, p. 1828, 1985.

[12] N. Alemdaroglu, I. Iyigun, M. Altun, H. Uysal, F. Quagliotti, and G. Guglieri, "Determination of dynamic stability derivatives using forced oscillation technique," in *40th AIAA Aerospace Sciences Meeting & Exhibit*, p. 528, 2002.

[13] A. Davari and M. Soltani, "Effects of plunging motion on unsteady aerodynamic behavior of an aircraft model in compressible flow," 2007.

[14] E. Oktay and H. Akay, "Cfd predictions of dynamic derivatives for missiles," in *40th AIAA aerospace sciences meeting & exhibit*, p. 276, 2002.

[15] S. Schmidt and D. M. Newman, "Estimation of dynamic stability derivatives of a generic aircraft," in *Proceedings of the 17th Australasian Fluid Mechanics Conference*, 2010.

[16] A. D. Ronch, D. Vallespin, M. Ghoreyshi, and K. Badcock, "Evaluation of dynamic derivatives using computational fluid dynamics," *AIAA journal*, vol. 50, no. 2, pp. 470–484, 2012.

[17] M. Baigang, Z. Hao, and W. Ban, "Computational investigation of simulation on the dynamic derivatives of flight vehicle," in *29th Congress of the International Council of the Aeronautical Sciences*, pp. 1–7, ICAS St. Petersburg, Russia, 2014.

[18] A. Despeyroux, J.-P. Hickey, R. Desaulnier, R. Luciano, M. Piotrowski, and N. Hamel, "Numerical analysis of static and dynamic performances of grid fin controlled missiles," *Journal of Spacecraft and Rockets*, vol. 52, no. 4, pp. 1236–1252, 2015.

[19] T. D. Economon, F. Palacios, S. R. Copeland, T. W. Lukaczyk, and J. J. Alonso, "Su2: An open-source suite for multiphysics simulation and design," *Aiaa Journal*, vol. 54, no. 3, pp. 828–846, 2016.

[20] J. Donea, A. Huerta, J.-P. Ponthot, and A. Rodríguez-Ferran, "Arbitrary lagrangian–eulerian methods," *Encyclopedia of computational mechanics*, 2004.

[21] F. Palacios, T. D. Economon, A. Aranake, S. R. Copeland, A. K. Lonkar, T. W. Lukaczyk, D. E. Manosalvas, K. R. Naik, S. Padron, B. Tracey, *et al.*, "Stanford university unstructured (su2): Analysis and design technology for turbulent flows," in *52nd Aerospace Sciences Meeting*, p. 0243, 2014.

[22] P. Spalart and S. Allmaras, "A one-equation turbulence model for aerodynamic flows," in *30th aerospace sciences meeting and exhibit*, p. 439, 1992.

[23] F. Menter, "Zonal two equation kw turbulence models for aerodynamic flows," in *23rd fluid dynamics, plasmadynamics, and lasers conference*, p. 2906, 1993.

[24] F. Palacios, J. Alonso, K. Duraisamy, M. Colonno, J. Hicken, A. Aranake, A. Campos, S. Copeland, T. Economon, A. Lonkar, *et al.*, "Stanford university unstructured (su 2): an open-source integrated computational environment for multi-physics simulation and design," in *51st AIAA aerospace sciences meeting including the new horizons forum and aerospace exposition*, p. 287, 2013.

[25] A. E. Series, "Introduction to dynamics and control of flexible structures," *JL Junkins*.